Conformation of von Willebrand factor in shear flow revealed with stroboscopic single-molecule imaging

Hans Bergal (Boston Children's Hospital, United States) Yan Jiang (Boston Children's Hospital, United States) Darren Yang (Wyss Institute, United States) Timothy Springer (Boston Children's Hospital, United States) Wesley Wong (Boston Children's Hospital and Harvard Medical School, United States)

Abstract:
von Willebrand factor (VWF) is a multimeric blood protein that acts as a mechanical probe, responding to changes in flow to initiate platelet plug formation. Previously, our labs had shown using single-molecule imaging that shear stress can extend surface-tethered VWF, but paradoxically we found that the required shear stress was higher than reported for free-in-flow VWF—an observation inconsistent with basic physical principles. To resolve this inconsistency critical to VWF's molecular mechanism, we measured free VWF extension in shear flow using PULSIS—**Pu**lsed **L**aser **S**troboscopic **I**maging of **S**ingle molecules. Here, laser pulses of different durations are used to capture multiple images of the same molecule within each frame, enabling accurate length measurements in the presence of motion blur. At high shear stresses, we observed a mean shift in VWF extension of less than 200 nm, much shorter than the multiple-micron extensions previously reported with no evidence for the predicted sharp globule-stretch conformational transition. Modeling VWF with a Brownian dynamics simulation, our results are consistent with VWF behaving as an uncollapsed polymer rather than the theorized compact ball. The muted response of free VWF to high shear rates implies that 1) the tension experienced by free VWF in physiological shear flow is lower than indicated by previous reports and 2) that tethering to platelets or the vessel wall is required to mechanically activate VWF adhesive function for primary hemostasis.

Conflict of interest: No COI declared

COI notes:

Preprint server: No;

Author contributions and disclosures: H.T.B., W.P.W., Y.J., and D.Y designed the research. H.T.B and Y.J. performed the experiments. H.T.B and D.Y ran simulations. W.P.W and H.T.B. drafted the manuscript. W.P.W., D.Y, Y.J, and H.T.B. analyzed data. H.T.B., Y.J., D.Y., T.A.S., and W.P.W. discussed the results and commented on the manuscript.

Non-author contributions and disclosures: No;

Agreement to Share Publication-Related Data and Data Sharing Statement: Email to the corresponding author

Clinical trial registration information (if any):

1 **Conformation of von Willebrand factor in shear flow revealed with stroboscopic single-molecule**
2 **imaging**

3 Hans T. Bergal[1-3], Yan Jiang[2-4], Darren Yang[2,3,5], Timothy A. Springer[2-4], and Wesley P. Wong[2-5*]

4 Affiliations:
5 [1]Harvard Biophysics; [2]Program in Cellular and Molecular Medicine, Boston Children's Hospital;
6 [3]Department of Biological Chemistry and Molecular Pharmacology, Blavatnik Institute at Harvard
7 Medical School; [4]Department of Pediatrics, Harvard Medical School; [5]Wyss Institute for Biologically
8 Inspired Engineering, Harvard University
9
10
11 *Correspondence: Wesley P. Wong, Center for Life Sciences, 3rd floor, Boston Children's Hospital, 3
12   Blackfan Circle, Boston, MA 02215; e-mail: wesley.wong@childrens.harvard.edu

13 Word counts for text: 3976

14 Word counts for abstract: 228

15 Figure count: 4

16 Reference count: 67

Key points:

- Free von Willebrand factor in flow extends gradually as shear stress increases, not abruptly with the presumed globule stretch transition.
- Polymer simulations suggest that VWF behaves as an uncollapsed, random chain with minimal monomer-monomer interactions.

Abstract:

von Willebrand factor (VWF) is a multimeric blood protein that acts as a mechanical probe, responding to changes in flow to initiate platelet plug formation. Previously, our labs had shown using single-molecule imaging that shear stress can extend surface-tethered VWF, but paradoxically we found that the required shear stress was higher than reported for free-in-flow VWF—an observation inconsistent with basic physical principles. To resolve this inconsistency critical to VWF's molecular mechanism, we measured free VWF extension in shear flow using PULSIS—**Pu**lsed **L**aser **S**troboscopic **I**maging of **S**ingle molecules. Here, laser pulses of different durations are used to capture multiple images of the same molecule within each frame, enabling accurate length measurements in the presence of motion blur. At high shear stresses, we observed a mean shift in VWF extension of less than 200 nm, much shorter than the multiple-micron extensions previously reported with no evidence for the predicted sharp globule-stretch conformational transition. Modeling VWF with a Brownian dynamics simulation, our results are consistent with VWF behaving as an uncollapsed polymer rather than the theorized compact ball. The muted response of free VWF to high shear rates implies that 1) the tension experienced by free VWF in physiological shear flow is lower than indicated by previous reports and 2) that tethering to platelets or the vessel wall is required to mechanically activate VWF adhesive function for primary hemostasis.

Introduction

von Willebrand factor (VWF) is a multimeric glycoprotein that circulates in blood and helps regulate hemostasis[1,2]. Consisting of 40-250 monomeric units arranged end-to-end, each VWF concatemer can have a contour length up to 15 µm[3–5]. Hydrodynamic forces regulate VWF's molecular mechanisms via tension-dependent binding. Binding partners include GPIbα for platelet recruitment[6–10], collagen for immobilization to damaged blood vessels[11,12], other VWF molecules for amplifying activation[13–15], and ADAMTS13 protease for VWF size-regulation[15–19]. VWF activation is premised upon its sensitivity to force, with conformational changes expected above a critical shear threshold. Extension is thought to expose binding sites, but sufficient tension is also required to allosterically activate binding to recruit platelets and initiate hemostasis.

Recently, Fu et al.[6] tethered VWF to a surface and measured VWF response to shear flow at the single-molecule level, monitoring extension and ability to bind the platelet-protein GP1bα. Surface-tethered VWF (figure 1A red) showed shear-dependent increases in extension up to the maximum shear stress applied (1280 dyn/cm^2). For reference, normal arterial shear stress is between 10-70 dyn/cm^2 but is estimated to reach higher than 400 dyn/cm^2 in injured arterioles[20].

In an earlier study[21], free VWF in pure shear flow was directly imaged. There appeared to be an extension of free VWF from a collapsed ball to an elongated filament ~15 µm in length, with abrupt extension at ~50 dyn/cm^2. Vascular injury was proposed to increase shear stress above this critical threshold, causing free-in-flow VWF to extend and adhere to the vessel wall at injury sites. A coarse-grained polymer model calibrated to match the extending behavior was used to model VWF[21,22]. The basic model of a collapsed polymer has been subsequently updated to simulate VWF behavior on a surface[23–25], in elongational flow[26–28], in shear flow[29–31] and size regulation through enzymatic cleavage[17,32,33].

These tethered and free VWF single-molecule experiments present a paradox: the putative shear stress required to extend free VWF was *lower* than the shear stress required to extend surface-tethered VWF (figure 1B). Simulations (figure 1C), based on Schneider et al's[21] model were applied to both free and surface-tethered scenarios. They predict surface-tethered VWF should extend at shear stresses 100x lower than free VWF. Independent of simulations, basic physical arguments predict a lower shear stress to extend tethered vs. free polymers[30,34,35].

To resolve this discrepancy, we experimentally investigated the response of free VWF in shear flow using a new method to properly account for motion blur. Additionally, we updated the coarse-grained polymer model to match our new results and previously published single-molecule experiments. We find an uncollapsed polymer is sufficient to describe mesoscopic VWF behavior in flow, which complements a recent study that found evidence for a random coil description of VWF[36]. In contrast, models representing VWF as a collapsed polymer are difficult to reconcile with single-molecule data.

Our results indicate that single molecules of free VWF in physiological shear flow experience much lower internal tension than previous experiments and models predicted. This has major consequences for understanding the molecular mechanisms of hemostasis initiation, including the tension-dependent activation of VWF binding in flow and VWF size regulation, and further clinical significance for von Willebrand disease (VWD), thrombotic thrombocytopenic purpura (TTP), and Heyde's syndrome[4].

3

79   **Methods**

80   **VWF and control preparation**

81   Recombinant, therapeutic grade VWF was size-fractionated to select for longer multimers and labeled
82   with Alexa 488 NHS-ester as described in Fu et al[6]. For the positive control, M13mp18RF DNA was
83   labeled with YOYO-1. Fluorescent beads (diameter=0.11 μm determined by manufacturer) were used for
84   the negative control. Imaging buffer was 60% (w/w) sucrose with 20 mM HEPES (pH 7.4), 150 mM NaCl,
85   0.02% Tween-20 and 0.5 mg/ml BSA.

86   **Pulsed Laser Stroboscopic Imaging of Single molecules (PULSIS)**

87   Molecules were imaged with a lab built TIRF microscope (60x oil immersion objective). A pressure-
88   driven flow system was used to flow VWF through microfluidic channels (figure 2A). To correct for
89   motion blur, we developed PULSIS (figure 2B-D), which images each molecule multiple times with
90   different duration laser pulses. This enables us to build a relationship between the laser pulse duration
91   and the observed streak length on a per molecule basis which is used to determine a "zero-pulse" or
92   motion blur corrected length. Molecules were imaged with pulsed laser illumination, which followed a
93   pattern of 1-on,3-off,1-on,3-off,2-on,3-off,3-on,3-off with the frequency of the pulse pattern tuned to
94   the fluid velocity. (See supporting text section 1).

95   **Image Analysis**

96   PULSIS trajectories were analyzed with custom MATLAB scripts. Trajectories were manually selected,
97   streak lengths were measured, and pulse duration (1,2,3) was assigned. A linear regression of pulse
98   duration and measured lengths with fitting errors was performed, giving the particle velocity (slope) and
99   the corrected molecule length (y-intercept).

100   **Simulation**

101   VWF multimers are represented by spherical beads, connected by a finitely extensible nonlinear elastic
102   (FENE) potential with relevant hydrodynamic interactions[22]. Bead positions are updated according to a
103   discretized Langevin equation based on the applied forces and random fluctuations from Brownian
104   motion. The simulation uses a non-specific Lennard-Jones (LJ) potential, which accounts for a cohesive
105   monomer-monomer attraction and excluded volume. (See supporting text S2).

106   **Data Sharing**

107   For data, contact wesley.wong@childrens.harvard.edu

108   **Results**

109   **Pulsed Laser Stroboscopic Imaging of Single molecules (PULSIS)**

110   To resolve the discrepancy between force scales of free and tethered VWF experiments, we developed a
111   new single-molecule approach to investigate the length response of free VWF to shear flow. The primary
112   experimental challenge is accurately measuring the lengths of molecules rapidly flowing through the
113   field of view. The movement of molecules during image exposure causes motion blur, which is difficult
114   to distinguish from molecule extension.

115 To correct motion blur at high shear rates we developed PULSIS, which images each molecule multiple
116 times using a series of different duration laser pulses (figure 2A,B). The pulse pattern creates a series of
117 fluorescent streaks that encode the length and velocity (dependent on distance from the vessel wall) of
118 the molecule within a single frame. Based on the pulse duration and measured streak lengths, a linear
119 regression gives the particle velocity (slope) and the length for a "zero-duration" pulse (y-intercept), i.e.,
120 the true length of the molecule. Example experimental PULSIS trajectories (figure 2C) show a
121 fluorescently-labeled DNA molecule flowing across a single frame illuminated with the laser pulse
122 pattern. The measured streak lengths at the corresponding pulse durations are fit to a line (streak length
123 vs pulse duration), with the corrected extension given by the y-intercept (figure 2D). The corresponding
124 linear fits of the image trajectories in figure 2C show linearized M13 DNA captured in two different
125 orientations that differ in apparent length during tumbling in shear flow.

126 To test if PULSIS can distinguish between compact and elongated particles, we measured fluorescently
127 labeled double-stranded DNA, in both the supercoiled and linearized states (figure 2E). Each molecule
128 gives a motion-blur corrected length; these are aggregated together to build up a distribution of lengths
129 (figure 2E). For example, the two trajectories (figure 2C-D) are single statistics from the distribution for
130 linearized DNA in figure 2E. Supercoiled DNA remained compacted, giving a normal distribution with
131 mean length L=0.26±0.25 µm. In contrast, linearized DNA had a broader distribution, with molecules up
132 to ~1.7 µm and a shifted mean length L=0.58±0.38 µm, comparable to expected distributions for DNA in
133 shear flow[37]. Broadening of the length distribution arises from the rotational component of shear flow,
134 which causes polymers to tumble in cycles of extension and relaxation[38], with sampling of these states
135 resulting in a broad distribution. To further validate PULSIS, fluorescent beads were imaged at shear
136 stresses between 20-200 dyn/cm^2 (figure 2F). The average measurement at each shear stress was within
137 10 nm of the manufacturer's reported diameter of 110 nm and had no dependence on the applied shear
138 stress.

139 Distinguishing collapsed vs. extended free-VWF can be difficult due to motion blur. One approach
140 imaged fiduciary beads to subtract out motion-blur effects for VWF in shear flow[21]. However, small
141 deviations in distance from the flow vessel wall between molecules and their fiducials (even less than
142 the depth of field, supporting text S3) can result in large errors in perceived VWF length. In contrast,
143 PULSIS uses each molecule as its own reference, without requiring comparison to other objects or
144 precise knowledge of distance from the surface. Another approach used single short-illumination pulses
145 to minimize the motion blur of VWF in flow[39]. However, this method has limited signal-to-noise ratio
146 and retains some motion blur artifacts. By contrast, PULSIS can fully account for motion blur by
147 extrapolation to infinitesimally short pulses while maintaining a strong signal-to-noise ratio. While
148 others have used short, stroboscopic pulses to limit motion blur and track molecules[39–41], to our
149 knowledge PULSIS is novel in using a pattern of different duration pulses to measure molecule lengths in
150 flow.

151 Additionally, we used a 60% (w/w) sucrose solution to increase the viscosity of the imaging buffer by
152 ~58 times compared to water[42] to study higher shear rates. This high-viscosity buffer applies equivalent
153 shear stress at a 58-fold lower flow rate with correspondingly lower motion blur[6,39]. Surface-tethered
154 VWF was imaged in both aqueous buffer and high-viscosity sucrose buffer at equivalent applied shear
155 stresses (figure S2)[6]. Similar to previous studies[7], no differences in length were observed between
156 molecules in the aqueous and sucrose buffer at the same shear stress, suggesting sucrose has minimal
157 effects on the energetics of VWF extension. With the sucrose buffer and PULSIS, we can measure the

5

158   lengths of free VWF molecules at shear stresses up to 200 dyn/cm^2, double the limit of previous
159   experiments[39].

Measurement of VWF free in shear flow

161   Purified, fluorescently labeled VWF molecules were imaged with PULSIS at shear stresses of 20-200
162   dyn/cm^2(figure 3A), ranging from low arterial to pathological shear stresses[43]. Above 200 dyn/cm^2, the
163   signal-to-noise ratio was too low for reliable data. However, this is still twice the highest shear stress
164   imaged in previous studies of VWF free in flow[39]. The underlying size-distribution of VWF was estimated
165   based on the length of tethered VWF molecules, with some molecules at least 6 µm in length (figure
166   S2B).

167   At the lowest shear stress, the measured length distribution was Gaussian with mean and standard
168   deviation L=0.15±0.17 µm. We interpret this distribution as containing compact VWF molecules, with
169   the variance resulting primarily from measurement error. At 50 dyn/cm^2, the measured mean increased
170   by 30 nm to 0.18 µm, dramatically less than the ~10 µm increase suggested[21] (figure 3B). At 200
171   dyn/cm^2, the highest shear stress measured, the mean length had shifted to 0.29 µm. Between 20 and
172   200 dyn/cm^2, the standard deviation increased from 0.16 to 0.41 µm, indicating the distributions were
173   broadening. Like linearized DNA, the length distributions broaden at higher shear stresses as the VWF
174   tumbles. The distributions are convolutions of the measurement error, the underlying VWF size
175   distribution, and the tumbling of individual molecules.

176   The distributions at each shear stress were compared using the nonparametric Mann-Whitney U test for
177   statistical significance. The test calculates the probability that the length distributions at two given
178   shears are the same (figure 3D). Distributions at similar shear (80 dyn/cm^2 vs. 100 dyn/cm^2) are
179   statistically similar (p=0.91). Large changes in shear stress, for example, 50 vs. 150 dyn/cm^2, give
180   statistically different distributions (p<0.001), indicating the length distribution changes a marginal but
181   statistically significant amount over the shear range explored.

182   We observed a small population of VWF molecules with a measured length of ~2 µm (figure 3A, E-F),
183   consistent with length heterogeneity in the VWF concatemers and suggesting some elongation in this
184   subset at 100-200 dyn/cm^2. Comparing the 90th percentile of lengths between the 20 and 200 dyn/cm^2
185   shear stresses demonstrates a doubling in length (350 to 800 nm), while the median length changes by
186   <100 nm (figure 3C).

Brownian Dynamics polymer simulations for VWF

188   Previous attempts to model VWF in flow have relied on coarse-grained Brownian Dynamics polymer
189   simulations, as the massive size of VWF and the long timescales of physiological processes make full MD
190   simulations unfeasible. The original free VWF in shear studies put forth a widely used Brownian
191   dynamics model[22]. With more single-molecule experiments for VWF, we now have orthogonal
192   experiments to test the model against[6,24,39].

193   The two parameters u (Lennard-Jones (LJ) interaction strength) and r (bead radius), make up a phase
194   space which represents possible realizations of the simulation (figure 4A). Used to model basic
195   intermolecular interactions[44], the Lennard-Jones potential is non-specific, meaning beads interact with
196   all other beads. The LJ well-depth determines the strength of intermolecular interactions. With a large
197   value (u> 0.314 k$_B$T), beads favorably interact to form a collapsed globule resistant to extension up to a

6

198   critical shear stress, above which a sudden globule-stretch transition occurs[22,30,35]. VWF was proposed to
199   behave like a collapsed polymer because a sharp transition was reported to occur in shear flow[21]. The
200   simulation has been updated in more recent work to include features like A2 unfolding but continues to
201   use collapsed polymers with LJ potentials between 0.52-1.44 k_BT [23–25,29,45].

202   At smaller interaction potentials (u<0.314 k_BT), a polymer behaves as an uncollapsed polymer. At the Θ-
203   point (u=0.314 k_BT), the attractive and repulsive forces cancel out, and the polymer's dimensions match
204   that of a simple ideal chain[46,47]. Unlike a collapsed polymer, an uncollapsed polymer's extension changes
205   smoothly with increasing shear and does not have a sharp transition[38,48].

206   Shear resistance is also dependent on bead size. Larger beads experience more hydrodynamic drag than
207   smaller beads causing elongation at lower shear stresses. In the original model, a large monomer
208   attraction was used to get a sharp transition, which required a large bead of r=80 nm to fit the critical
209   shear stress. Based on EM images from Fowler et al.[49] (figure 4B) and x-ray crystallography structures[1], a
210   spherical radius of 80 nm overestimates two dimensions of VWF monomers. Recent models have
211   attempted to correct this and reduced the bead radius to r=10-15 nm [23–25,29,45] but still overestimate the
212   cross-section of VWF monomers (figure 4B).

213   We tested a polymer at the Θ-point (u=0.314 k_BT) and optimized the bead size to best match the single-
214   molecule experiments described below and found a radius of r=3.7 nm. This radius would require 8
215   spherical beads to make up a full monomer of 60 nm [49]. Notably, this bead size is similar to the size of
216   the 11 domains in each VWF monomer, which range from 1.5-3 nm in radius[1,50]. We also evaluated the
217   original Brownian dynamics model (u=2.08 k_BT, r=80 nm) [21,22] and a revised-LJ model (*u*=2.08 k_BT, r=14
218   nm) with a smaller radius representative of recent models[23–25,45]. The simulations are compared to three
219   single-molecule experiments: previous measurements of surface-tethered VWF stretching in shear flow
220   and subsequent relaxation[6] and measurements here of free VWF in shear flow. All simulations have a
221   contour length of ~3 μm based on the average maximum extension length from surface extension
222   experiments (figure S2B, expanded lengths in figures S3-4,S7,S9).

223   **Polymer simulations for surface-tethered VWF in shear flow**

224   Surface-tethered VWF in shear flow was simulated with the three models described above.
225   Experimental data from Fu et al.[6] shows VWF extends little between 10-40 dyn/cm^2. Between 40-1280
226   dyn/cm^2, VWF requires an exponential increase in shear to achieve a linear length increase. Shear flow
227   was applied to the tethered polymer models, then length in the flow direction was recorded and
228   normalized by the length at the highest shear stress. When normalized by maximum extension, shear-
229   extension curves of VWF are generally independent of length[6].

230   With a small bead size, our uncollapsed polymer experiences less hydrodynamic extensional force than
231   other models and entropic effects are sufficient to resist extension without a cohesive potential. Like
232   VWF, the simulated uncollapsed polymer's fractional extension scales logarithmically with shear stress
233   and matches the data well (figure 4c). In contrast, due to large beads, the original LJ model unfolds
234   completely by 10 dyn/cm^2 when tethered to the surface, at a shear stress ~100 times lower than
235   experimentally observed. Furthermore, independent of bead radius, models with strong LJ interactions
236   extend abruptly over a narrow range of shear stresses[22,35]. The revised-LJ model was optimized to reach
237   the proper half-maximal extension at the same shear as VWF. This collapsed polymer extends ~65% of

7

238 its maximal length between 160 and 320 dyn/cm^2, showing an abrupt transition not experimentally
239 observed.

Polymer simulations for free VWF in shear flow

241 The polymer simulations were further compared to our experimental measurements here of free VWF
242 in shear flow. Shear flow was applied and the length distribution over time was recorded, as measured
243 by the maximum length difference along the axis of flow. Since the contour length of the experimental
244 VWF data is not known, the lengths are not normalized. The experimental data also represents a
245 heterogenous distribution of sizes, making direct comparison difficult as polymer simulations have
246 shown a size dependence for elongation in shear stress[30,51]. However, the qualitative behavior of each
247 model is still informative.

248 Mean extensions of the simulated polymers in free shear were compared to the mean experimental
249 length measurements (figure 4D). The original LJ model was specifically designed to exhibit large
250 conformational changes in mean extension at shear stresses around 50-80 dyn/cm^2 and predicts a mean
251 length change of 0.8 µm. The revised-LJ model, with parameters set to match the experimental surface
252 stretching data, has a critical shear rate higher than the experiment and shows no change in mean
253 length in the tested range. Our uncollapsed polymer model increases in mean extension by ~150 nm
254 between 40-160 dyn/cm^2, qualitatively matching the observed behavior. Based on the uncollapsed
255 polymer model, the mean tension under physiological shear stress was estimated to be <0.1 pN
256 (supporting text S4, figure S5).

Polymer simulations for VWF relaxation

258 Polymer relaxation in the absence of flow provides orthogonal experimental VWF data to further test
259 the predictions of models. Relaxation provides details on timescale and conformation. Experimental
260 data was analyzed from Fu et al.[6] where VWF in a high-viscosity sucrose buffer is hydrodynamically
261 stretched by a high shear stress and imaged as the molecule relaxes. Even in high viscosity buffer, VWF
262 relaxes quickly in ~1 second. In our simulations (supporting text S5), we find the relaxation time scale is
263 inversely correlated with the polymer bead size, consistent with a small bead radius to parameterize
264 VWF (figure S6,S7). Furthermore, the relaxation conformation, based on the experimental fluorescence
265 distribution of VWF, disagrees with the collapsed polymer simulation but is well-modeled by our
266 uncollapsed polymer simulation (figure S8,S9).

Discussion

268 We developed PULSIS, an approach for measuring the lengths of molecules in high shear flow by
269 measuring each molecule multiple times with different duration pulses. We then investigated VWF at
270 shear stresses ranging from 20-200 dyn/cm^2, representing physiological to pathological shear stresses to
271 capture relevant changes *in vivo*[20]. Qualitatively, the VWF length distribution shows no sharp globule-
272 stretch transition near the previously reported 50 dyn/cm^2 threshold. Quantitatively, the change in
273 mean length between 20-200 dyn/cm^2 is two orders of magnitude less than the previously reported
274 values (0.17 vs 13 µm)[21]. This discrepancy may have resulted from motion blur artifacts in the previous
275 work[21]. High shear rates coupled with limited axial resolution would make it difficult to account for
276 motion blur with fiducial beads.

8

277   The small response of VWF to pure shear flow is a departure from the current perception within the
278   field but still consistent with a majority of VWF literature. Length distributions, with a long tail with low
279   micrometer lengths, is consistent with VWF free-in-flow experiments from Vergauwe et al.[39].
280   Furthermore, the measured mean extension of free VWF is less than the extension of tethered VWF
281   reported by Fu et al.[6] at the same shear stress, resolving the force paradox discussed in figure 1B. A
282   small response of VWF to shear stress is also consistent with small-angle neutron scattering
283   experiments[52] which found no large-scale rearrangement at 30 dyn/cm^2 as well as dynamic light
284   scattering experiments[7] which found no evidence for individual VWF extension at 60 dyn/cm^2.

285   Tension allosterically activates VWF binding to platelet proteins GPIb[6]. Furthermore, VWF cleavage by
286   ADAMTS13 requires unfolding of the A2 domain for monomer cleavage, indicating that tension helps
287   regulate VWF function[16]. Our results imply the tension experienced by free VWF in shear flow is lower
288   than previously assumed; since tension depends on the difference in velocity between opposing ends of
289   the molecule, a smaller extension should result in a comparably smaller tension[53].

290   Studies have observed VWF cleavage accelerated with shear stress[17,54]. However, other studies have
291   observed no increase in ADAMTS13 cleavage with either high shear or elongational flow[55] but find that
292   high turbulent flow results in VWF cleavage[56]. Based on our polymer model, the average tension at 80
293   dyn/cm^2, high arterial stress, is estimated to be <0.1 pN (figure S5), much lower than the force scale
294   measured for A2 unfolding (f_b=1.1±0.2 pN)[16]. The estimated tension predicts that physiological shear
295   does not dramatically bias on average the unfolded form of free-VWF A2 for VWF cleavage. However, it
296   is unconfirmed whether physiological force could still play a role in accelerating the rate of cleavage or
297   create a preference for cleavage of longer VWF molecules. The exact flow conditions and contributions
298   from blood proteins like Factor VIII[60] needed for VWF cleavage require further experimental
299   investigation.

300   VWF localizes to the area of vascular injury and recruits other clotting factors like platelets. VWF
301   localization is likely driven by binding to collagen in the vessel wall that is exposed in injury[1]. Both flow-
302   dependent[12] and flow-independent[61,62] VWF-collagen binding have been reported. Injury could expose
303   collagen in the endothelium, allowing binding independent of flow. If the VWF-collagen binding rate has
304   some tension dependence, shear stresses below 200 dyn/cm^2 are not predicted to have a significant role
305   in accelerating binding. Supporting this, Colace and Diamond[12] observed minimal rates of VWF-collagen
306   binding at a shear stress of 125 dyn/cm^2.

307   Extension and tension (~20 pN)[6] are necessary to shift the VWF A1 domain from a low affinity to a high
308   affinity state for platelet protein GP1b binding[6]. Our results suggest single-molecules of free VWF alone
309   do not exhibit shear-stress dependent binding to GP1b at physiological shear rates. Recruitment of
310   platelets is likely only after VWF is attached to a surface, where the flow directly stretches VWF and
311   higher tensions are reached. Interestingly, Nesbitt et al.[63] predominantly observed platelet aggregation
312   on vessel walls at the point of stenosis, supporting the idea that both high flow and surface attachments
313   are important for platelet aggregation.

314   We found no evidence for the sharp transition for free-in-flow VWF predicted by the LJ collapsed
315   polymer simulations. Furthermore, based on the relaxation conformation and surface stretching
316   behavior, the LJ collapsed polymer is not a suitable model for VWF. Meanwhile, our uncollapsed
317   polymer model was consistent with previous VWF surface stretching-in-flow experiments[6], our own
318   PULSIS data for free polymers in shear, and both time scale and conformation of relaxation from a

9

stretched state. While the good agreement of single-molecule experiments with our uncollapsed polymer models do not constitute proof, an uncollapsed polymer is a sufficient description of the observed mesoscopic VWF dynamics in flow. Optimal bead size is on a similar scale as VWF domains, giving further agreement with physical observations of VWF. Our model suggests that VWF does not adopt a globular, collapsed form and monomers have minimal attractive interactions. This supports recent ultracentrifuge experiments where VWF behaved like a random coil[36] and is consistent with EM images of VWF[49].

The molecular mechanism of VWF activation is based on large conformational changes above a critical shear threshold to initiate hemostasis. However, we find no experimental evidence for a critical shear for large conformational changes in free-in-flow VWF—observed length changes are ~10 times smaller than previously thought. We find gradual length changes over a range of shear stress, consistent both in scale and shape with an uncollapsed polymer. Our results suggest free-flowing VWF molecules cannot act as a responsive sensor of shear stress for activation of hemostasis, invalidating a commonly held view of VWF activation. The field should investigate alternative initiation mechanisms, including the role of elongational flow near constriction sites, flow-independent binding to collagen in the vessel wall, and interaction with platelets.

Acknowledgements

Author contributions

H.T.B., W.P.W., Y.J., and D.Y designed the research. H.T.B and Y.J. performed the experiments. H.T.B and D.Y ran simulations. W.P.W and H.T.B. drafted the manuscript. W.P.W., D.Y, Y.J, and H.T.B. analyzed data. H.T.B., Y.J., D.Y., T.A.S., and W.P.W. discussed the results and commented on the manuscript.

Conflict-of-interest Disclosure

All the authors declare no competing financial interests.

ORCID profiles H.T.B., 0000-0002-5499-7833; Y.J., 0000-0002-2745-4323; D.Y., 0000-0002-2271-6910; T.A.S., 0000-0001-6627-2904; W.P.W., 0000-0001-7398-546X

References

1. Springer TA. von Willebrand factor, Jedi knight of the bloodstream. *Blood*. 2014;124(9):1412-1425. doi:10.1182/blood-2008-10-165621.

2. Yee A, Kretz CA. Von Willebrand factor: Form for function. *Semin Thromb Hemost*. 2014;40(1):17-27. doi:10.1055/s-0033-1363155

3. Sadler JE. Biochemistry and genetics of von Willebrand factor. *Annu Rev Biochem*. 1998;67:395-424. doi:10.1146/annurev.biochem.67.1.395

4. Sadler JE. New concepts in von Willebrand disease. *Annu Rev Med*. 2005;56:173-191. doi:10.1146/annurev.med.56.082103.104713

5. Reininger AJ. Function of von Willebrand factor in haemostasis and thrombosis. *Haemophilia*. 2008;14(SUPPL. 5):11-26. doi:10.1111/j.1365-2516.2008.01848.x

6. Fu H, Jiang Y, Yang D, Scheiflinger F, Wong WP, Springer TA. Flow-induced elongation of von Willebrand factor precedes tension-dependent activation. *Nat Commun*. 2017;8(1). doi:10.1038/s41467-017-00230-2

7. Shankaran H, Alexandridis P, Neelamegham S. Aspects of hydrodynamic shear regulating shear-induced platelet activation and self-association of von Willebrand factor in suspension. *Blood*. 2003;101(7):2637-2645. doi:10.1182/blood-2002-05-1550

8. Jiang Y, Fu H, Springer TA, Wong WP. Electrostatic steering enables flow-activated Von Willebrand factor to bind platelet glycoprotein, revealed by single-molecule stretching and imaging. *J Mol Biol*. 2019;431(7):1380-1396. doi:10.1016/j.jmb.2019.02.014

9. Dayananda KM, Singh I, Mondal N, Neelamegham S. von Willebrand factor self-association on platelet GpIbα under hydrodynamic shear: Effect on shear-induced platelet activation. *Blood*. 2010;116(19):3990-3998. doi:10.1182/blood-2010-02-269266

10. Interlandi G, Yakovenko O, Tu A, et al. Specific electrostatic interactions between charged amino acid residues regulate binding of von Willebrand factor to blood platelets. 2017;292:18608-18617. doi:10.1074/jbc.M117.797456

11. Fuchs B, Budde U, Schulz A, Kessler CM, Fisseau C, Kannicht C. Flow-based measurements of von Willebrand factor (VWF) function : Binding to collagen and platelet adhesion under physiological shear rate. *Thromb Res*. 2010;125(3):239-245. doi:10.1016/j.thromres.2009.08.020

12. Colace T V., Diamond SL. Direct observation of von Willebrand factor elongation and fiber formation on collagen during acute whole blood exposure to pathological flow. *Arterioscler Thromb Vasc Biol*. 2013;33(1):105-113. doi:10.1161/ATVBAHA.112.300522

13. Fu H, Jiang Y, Wong WP, Springer TA. Single-molecule imaging of von Willebrand factor reveals tension-dependent self-association. *Blood*. Published online 2021. doi:10.1182/blood.2021012595

14. Zhang C, Kelkar A, Neelamegham S. Von Willebrand factor self-association is regulated by the shear-dependent unfolding of the A2 domain. *Blood Adv*. 2019;3(7):957-968. doi:10.1182/bloodadvances.2018030122

15. Zheng Y, Chen J, Lopez JA. Flow-driven assembly of VWF fibre and webs in in vitro microvessels.

387   Published online 2015. doi:10.1038/ncomms8858

388   16.   Zhang X, Halvorsen K, Zhang C-Z, Wong WP, Springer T. Mechanoenzymatic Cleavage of the
389   Ultralarge Vascular Protein von Willebrand Factor. *Science (80-)*. 2009;324(June).

390   17.   Lippok S, Radtke M, Obser T, et al. Shear-Induced Unfolding and Enzymatic Cleavage of Full-
391   Length VWF Multimers. *Biophys J*. 2016;110(3):545-554. doi:10.1016/j.bpj.2015.12.023

392   18.   Dong J fei, Moake JL, Nolasco L, et al. ADAMTS-13 rapidly cleaves newly secreted ultralarge von
393   Willebrand factor multimers on the endothelial surface under flowing conditions. *Blood*.
394   2002;100(12):4033-4039. doi:10.1182/blood-2002-05-1401

395   19.   Interlandi G, Ling M, Tu AY, Chung DW, Thomas WE. Structural Basis of Type 2A von Willebrand
396   Disease Investigated by Molecular Dynamics Simulations and Experiments. 2012;7(10).
397   doi:10.1371/journal.pone.0045207

398   20.   Malek AM, Alper SL, Izumo S. Hemodynamic Shear Stress and Its Role in Atherosclerosis. *JAMA*.
399   1999;282(21):2035-2042.

400   21.   Schneider SW, Nuschele S, Wixforth A, et al. Shear-induced unfolding triggers adhesion of von
401   Willebrand factor fibers. *Proc Natl Acad Sci*. 2007;104(19):7899-7903.
402   doi:10.1073/pnas.0608422104

403   22.   Alexander-Katz A, Schneider MF, Schneider SW, Wixforth A, Netz RR. Shear-flow-induced
404   unfolding of polymeric globules. *Phys Rev Lett*. 2006;97(13):1-4.
405   doi:10.1103/PhysRevLett.97.138101

406   23.   Morabito M, Dong C, Wei W, et al. Internal Tensile Force and A2 Domain Unfolding of von
407   Willebrand Factor Multimers in Shear Flow. *Biophys J*. 2018;115(10):1860-1871.
408   doi:10.1016/j.bpj.2018.09.001

409   24.   Wang Y, Morabito M, Zhang XF, Webb E, Oztekin A, Cheng X. Shear-Induced Extensional
410   Response Behaviors of Tethered von Willebrand Factor. *Biophys J*. 2019;116(11):2092-2102.
411   doi:10.1016/j.bpj.2019.04.025

412   25.   Dong C, Kania S, Morabito M, et al. A mechano-reactive coarse-grained model of the blood-
413   clotting agent von Willebrand factor. *J Chem Phys*. 2019;151(12). doi:10.1063/1.5117154

414   26.   Sing CE, Selvidge JG, Alexander-Katz A. Von Willlebrand adhesion to surfaces at high shear rates is
415   controlled by long-lived bonds. *Biophys J*. 2013;105(6):1475-1481. doi:10.1016/j.bpj.2013.08.006

416   27.   Kania S, Oztekin A, Cheng X, Zhang XF, Webb EB. Long time-scale study of von Willebrand factor
417   multimers in extensional flow. *bioRxiv*. Published online 2020:2020.09.09.290304.
418   https://doi.org/10.1101/2020.09.09.290304

419   28.   Kania S, Oztekin A, Cheng X, Zhang XF, Webb E. Predicting pathological von Willebrand factor
420   unraveling in elongational flow. *Biophys J*. 2021;120(10):1903-1915.
421   doi:10.1016/j.bpj.2021.03.008

422   29.   Ouyang W, Wei W, Cheng X, Zhang XF, Webb EB, Oztekin A. Flow-induced conformational change
423   of von Willebrand Factor multimer: Results from a molecular mechanics informed model. *J
424   Nonnewton Fluid Mech*. 2015;217:58-67. doi:10.1016/j.jnnfm.2015.01.009

425   30.   Alexander-Katz A, Netz RR. Dynamics and instabilities of collapsed polymers in shear flow.

426 *Macromolecules*. 2008;41(9):3363-3374. doi:10.1021/ma702331d

427 31. Alexander-Katz A. Toward novel polymer-based materials inspired in blood clotting.
428 *Macromolecules*. 2014;47(5):1503-1513. doi:10.1021/ma4007768

429 32. Huisman B, Hoore M, Gompper G, Fedosov DA. Modeling the cleavage of von Willebrand factor
430 by ADAMTS13 protease in shear flow. *Med Eng Phys*. 2017;48:14-22.
431 doi:10.1016/j.medengphy.2017.06.044

432 33. Radtke M, Lippok S, Rädler JO, Netz RR. Internal tension in a collapsed polymer under shear flow
433 and the connection to enzymatic cleavage of von Willebrand factor. *Eur Phys J E*. 2016;39(3).
434 doi:10.1140/epje/i2016-16032-7

435 34. Sing CE, Alexander-Katz A. Dynamics of collapsed polymers under the simultaneous influence of
436 elongational and shear flows. *J Chem Phys*. 2011;135(1). doi:10.1063/1.3606392

437 35. Buguin A, Brochard-Wyart F. Unwinding of globular polymers under strong flows.
438 *Macromolecules*. 1996;29(14):4937-4943. doi:10.1021/ma9600769

439 36. Parker ET, Lollar P. Conformation of the von Willebrand factor/factor VIII complex in quasi-static
440 flow. *J Biol Chem*. 2021;296:100420. doi:10.1016/j.jbc.2021.100420

441 37. Schroeder CM, Teixeira RE, Shaqfeh ESG, Chu S. Dynamics of DNA in the Flow-Gradient Plane of
442 Steady Shear Flow : Observations and Simulations. Published online 2005:1967-1978.
443 doi:10.1021/ma0480796

444 38. Smith DE, Babcock HP, Chu S. Single-polymer dynamics in steady shear flow. *Science (80-)*.
445 1999;283(5408):1724-1727. doi:10.1126/science.283.5408.1724

446 39. Vergauwe RMA, Uji-i H, Ceunynck K De, Vermant J, Vanhoorelbeke K, Hofkens J. Shear-Stress-
447 Induced Conformational Changes of von Willebrand Factor in a Water – Glycerol Mixture
448 Observed with Single Molecule Microscopy. Published online 2014. doi:10.1021/jp5022664

449 40. English BP, Hauryliuk V, Sanamrad A, Tankov S, Dekker NH, Elf J. Single-molecule investigations of
450 the stringent response machinery in living bacterial cells. *Proc Natl Acad Sci U S A*. 2011;108(31).
451 doi:10.1073/pnas.1102255108

452 41. Xie XS, Choi PJ, Li GW, Nam KL, Lia G. Single-molecule approach to molecular biology in living
453 bacterial cells. *Annu Rev Biophys*. 2008;37:417-444.
454 doi:10.1146/annurev.biophys.37.092607.174640

455 42. Lee JC, Timasheff SN. The stabilization of proteins by sucrose. *J Biol Chem*. 1981;256(14):7193-
456 7201. doi:10.1016/s0021-9258(19)68947-7

457 43. Sakariassen KS, Orning L, Turitto VT. The impact of blood shear rate on arterial thrombus
458 formation. 2015;1.

459 44. Lennard-Jones JE. Cohesion. *Proc Phys Soc*. 1931;43(5):461-482. doi:10.1088/0959-
460 5309/43/5/301

461 45. Wei W, Dong C, Morabito M, et al. Coarse-Grain Modeling of Shear-Induced Binding between von
462 Willebrand Factor and Collagen. *Biophys J*. 2018;114(8):1816-1829.
463 doi:10.1016/j.bpj.2018.02.017

464   46.   Graessley WW, Hayward RC, Grest GS. Excluded-Volume Effects in Polymer Solutions. 2.
465   Comparison of Experimental Results with Numerical Simulation Data. Published online
466   1999:3510-3517.

467   47.   Flory PJ. *Principles of Polymer Chemistry*. Cornell University Press; 1953.

468   48.   De Gennes PG. Coil-stretch transition of dilute flexible polymers under ultrahigh velocity
469   gradients. *J Chem Phys*. 1974;5030(August 2003):5030-5042. doi:10.1063/1.1681018

470   49.   Fowler WE, Erickson HP, Mckee PA, et al. Substructure of human von Willebrand factor .
471   Substructure of Human von Willebrand Factor. 1985;76(4):1491-1500.

472   50.   Dong X, Leksa NC, Chhabra ES, et al. The von Willebrand factor D'D3 assembly and structural
473   principles for factor VIII binding and concatemer biogenesis. *Blood*. 2019;133(14):1523-1533.
474   doi:10.1182/blood-2018-10-876300

475   51.   Schwarzl R, Netz RR. Hydrodynamic shear effects on grafted and non-grafted collapsed polymers.
476   *Polymers (Basel)*. 2018;10(8):27-30. doi:10.3390/polym10080926

477   52.   Singh I, Themistou E, Porcar L, Neelamegham S. Fluid shear induces conformation change in
478   human blood protein von Willebrand factor in solution. *Biophys J*. 2009;96(6):2313-2320.
479   doi:10.1016/j.bpj.2008.12.3900

480   53.   Shankaran H, Neelamegham S. Hydrodynamic Forces Applied on Intercellular Bonds, Soluble
481   Molecules, and Cell-Surface Receptors. *Biophys J*. 2004;86(1 I):576-588. doi:10.1016/S0006-
482   3495(04)74136-3

483   54.   Tsai H, Sussman I, Nagel R. Shear stress enhances the proteolysis of von Willebrand factor in
484   normal plasma. *Blood*. 1994;83(8):2171-2179. doi:10.1182/blood.v83.8.2171.2171

485   55.   Bortot M, Sharifi A, Ashworth K, et al. Pathologic Shear and Elongation Rates Do Not Cause
486   Cleavage of Von Willebrand Factor by ADAMTS13 in a Purified System. *Cell Mol Bioeng*.
487   2020;13(4):379-390. doi:10.1007/s12195-020-00631-2

488   56.   Bortot M, Ashworth K, Sharifi A, et al. Turbulent Flow Promotes Cleavage of VWF (von Willebrand
489   Factor) by ADAMTS13 (A Disintegrin and Metalloproteinase With a Thrombospondin Type-1
490   Motif, Member 13). *Arterioscler Thromb Vasc Biol*. 2019;39(9):1831-1842.
491   doi:10.1161/ATVBAHA.119.312814

492   57.   Soejima K, Nakamura H, Hirashima M, Morikawa W, Nozaki C, Nakagaki T. Analysis on the
493   molecular species and concentration of circulating ADAMTS13 in blood. *J Biochem*.
494   2006;139(1):147-154. doi:10.1093/jb/mvj013

495   58.   Zhang XF, Halverson K, Zhang C-Z, Wong WP, Springer TA. Mechanoenzymatic Cleavage of the
496   Ultralarge Vascular Protein von Willebrand Factor. 2009;(June).

497   59.   Batle J, Lopez-Fernandez MF, Lopez-Borrasca A, et al. Proteolytic Degradation Administration.
498   *Blood*. 1987;70(1):173-176.

499   60.   Cao W, Krishnaswamy S, Camire RM, Lenting PJ, Zheng XL. Factor VIII accelerates proteolytic
500   cleavage of von Willebrand factor by ADAMTS13. Published online 2008.
501   doi:10.1073/pnas.0801735105

502   61.   Machha V, Tischer A, Moon-Tasson L, Auton M. The von Willebrand Factor A1-Collagen III

503   Interaction is Independent of Conformation and Type 2 von Willebrand Disease Phenotype.
504   2017;429(1):32-47. doi:10.1016/j.jmb.2016.11.014.The

505 62.   Talpsep AKT. The von Willebrand factor collagen-binding activity assay : clinical application.
506   Published online 2001:466-471. doi:10.1007/s002770100329

507 63.   Nesbitt WS, Westein E, Tovar-Lopez FJ, et al. A shear gradient-dependent platelet aggregation
508   mechanism drives thrombus formation. *Nat Med*. 2009;15(6):665-673. doi:10.1038/nm.1955

509 64.   Humphrey W, Dalke A, Schulten K. {VMD} -- {V}isual {M}olecular {D}ynamics. *J Mol Graph*.
510   1996;14:33-38.

511 65.   York D, Evensen NM, Martínez ML, De Basabe Delgado J. Unified equations for the slope,
512   intercept, and standard errors of the best straight line. *Am J Phys*. 2004;72(3):367-375.
513   doi:10.1119/1.1632486

514 66.   Hill PD. Kernel Estimation of a Distribution Function. *Commun Stat - Theory Methods*.
515   1985;14(3):605-620. doi:10.1080/03610928508828937

516 67.   Silverman BW. *Density Estimation for Statistics and Data Analysis*.; 1986. doi:10.3311/PPme.8017

517

518

Figure Captions

Figure 1. Free vs surface tethered VWF extension under flow. **A** Diagram illustrating[64] free-in-flow VWF (blue) vs surface-tethered (red) with applied shear flow. **B** Data from Schneider et al.[21] (blue) showing normalized extension vs shear stress for free VWF and data from Fu et al.[6] (red) showing normalized extension vs shear for tethered VWF. Required shear stress for free VWF extension is expected to be higher than required shear stress for surface tethered extension but experimentally the opposite was observed. **C** Predictions of mean extension in response to shear stress based on a Brownian dynamics model with a strong Lennard-Jones interaction potential proposed by Schneider et al.[21] for both a free-in-flow (blue) and tethered (red) polymer. Lengths are normalized based on the maximum observed length in the direction of flow.

Figure 2. Pulsed Laser Stroboscopic Imaging of Single molecules (PULSIS). **A** Basic schematic of the pressure driven flow system and imaging set up, not to scale. **B** Cartoon depiction of PULSIS. Objects are imaged with different duration pulses and by comparing the relative lengths, we can accurately measure the lengths of moving objects, and distinguish point objects from elongated objects. **C** Example experimental PULSIS trajectories of fluorescently labeled linearized DNA at 50 dyn/cm^2. **D** Example relationship between measured length of pulse L_m (µm) vs relative pulse duration T_p (arbitrary time units) for the two DNA PULSIS trajectories in 2C. For each trajectory, streak lengths are measured and a linear regression performed of the form $L_m=L_0+V*T_p$ with fitting errors according to York et al[65]. L_m is the illuminated streak length that we measure and T_p is the relative pulse duration defined by the pulse pattern (1, 2, or 3). The linear fit gives us the particle velocity V, and the y-intercept L_0 represents the length of the molecule observed with an infinitesimally short pulse i.e with no motion blur. The first trajectory (yellow) has a corrected length of 0.29 µm and resembles a compact object. The second trajectory has a corrected length of 1.03 µm and represents an elongated object. Error bars on pulse length are based on goodness of fit to predicted pulse shape (Supplemental Methods). **E** Positive control showing histogram of PULSIS determined lengths of double stranded M13 DNA plasmid both in supercoiled (blue) and linearized (red) state at 50 dyn/cm^2 imaged in sucrose buffer. Histograms are of motion blur-corrected lengths of hundreds of single molecules. The examples (trajectories and analysis) from figure 2C-D are two statistics from the linearized (red) distribution. Histograms are displayed along with kernel density estimates. Kernel density estimation is a method for smoothing histograms by applying a gaussian kernel to each point[66]. A Gaussian kernel was used with bandwidth set by Silverman's rule[67] **F** Negative control showing kernel density estimate for PULSIS motion blur corrected beads at different shear stress (manufacture determined diameter of 0.11 µm). Raw histograms in figure S1. Number of measurements, mean length and standard deviation for each condition are shown in panels E and F.

Figure 3. Free-in-flow VWF extension in shear flow. **A** Histogram of VWF length at 6 shear stresses (20, 50, 80, 100, 150, 200 dyn/cm^2). **B** Mean extension vs shear stress (o) and standard deviation vs shear stress (Δ) of VWF molecules for histograms shown in 3A. Monotonic increases in mean and standard deviation are both consistent with molecules extending under flow. **C** Percentiles 50-90 of VWF length vs shear stress for histograms in 3A. **D** Nonparametric statistical significance testing using Mann-Whitney U test comparing each shear stress length distribution. Values for $p<0.05$ indicate statistical significance. **E** Three example trajectories of VWF at 150 dyn/cm^2 with different PULSIS corrected lengths. Example molecules of a long, middle, and short extended molecule. **F** Corresponding plots of

16

561 pulse length vs relative pulse duration for trajectories in fig 3E. The y-intercept represents motion blur
562 corrected lengths for VWF molecules.

563 **Figure 4. Comparison of Brownian dynamics models for VWF**. **A** Parameter space of the simulation as a
564 function of bead diameter and Lennard-Jones interaction strength. Comparison with the size of spheres
565 representing monomers of the different models. Sizes of spheres are on the same scale as 4B. Blue
566 space represents collapsed polymers, with yellow being uncollapsed polymers. Dotted line represents
567 the Θ-point where attractive and repulsive forces cancel out. **B** Electron microscopy images adapted
568 from Fowler et al.[49] of VWF. **C** Comparison between Brownian dynamics simulation and experimental
569 steady state extension for surface tethered polymers under shear flow. The three models are the
570 original Lennard-Jones model (◇), the revised Lennard-Jones model (Δ) and the uncollapsed polymer
571 model (▢). Simulations compared to experimental data from previous surface stretching experiments of
572 2-3.5 µm VWF molecules from Fu et al. (o, 156 molecules measured)[6]. For each model and shear stress,
573 the equilibrium extension of five independent simulations were averaged together at each shear stress.
574 Extension is normalized by maximum extension and plotted on a semi log plot. Shaded area shows
575 standard deviation of the 5 simulations. **D** Comparison of Brownian dynamics simulation and
576 experimental mean extension for free-in-flow VWF with applied shear flow as measured by PULSIS,
577 plotted on a semi log plot. Since the contour length of the experimental data is unknown, simulations
578 and data are not normalized. Polymer simulation extensions were averaged over a time window and
579 independent runs. (LJ original runs=3, Revised LJ runs = 3, Uncollapsed polymer runs = 10). Absolute
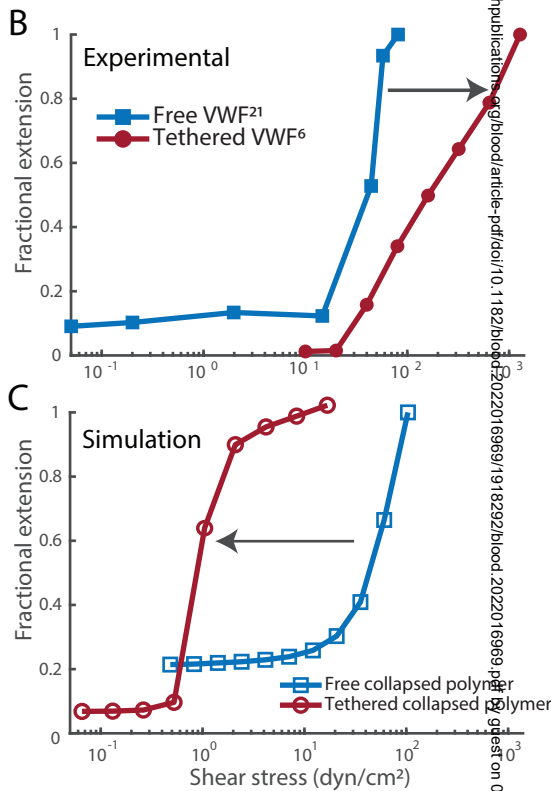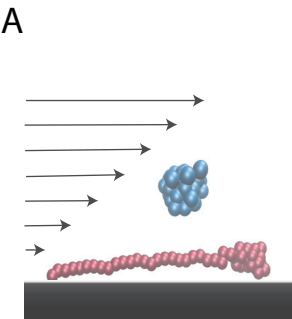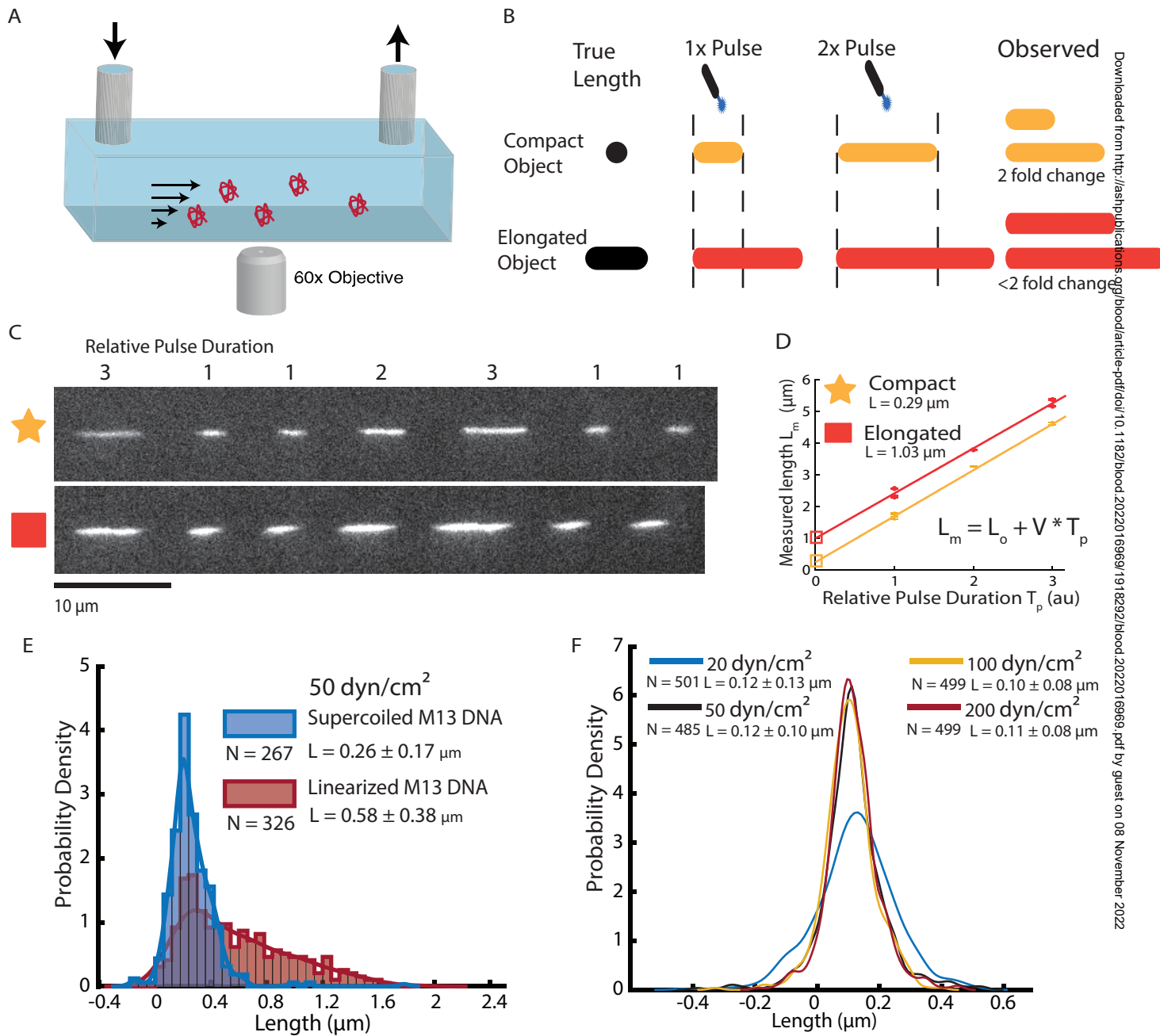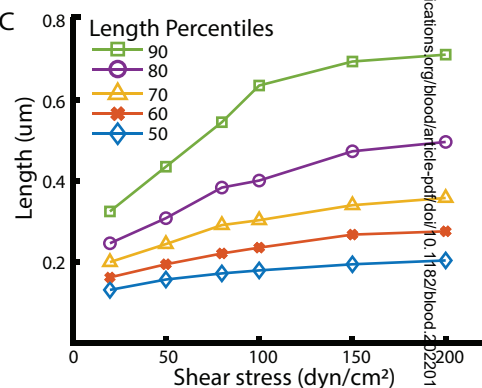580 contour length of all simulations was ~3 µm.
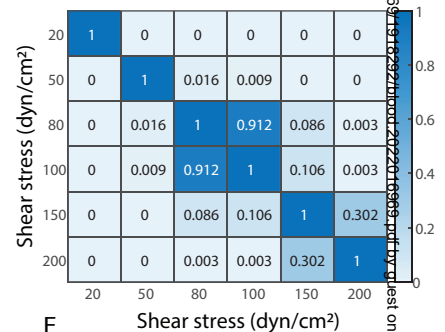
17
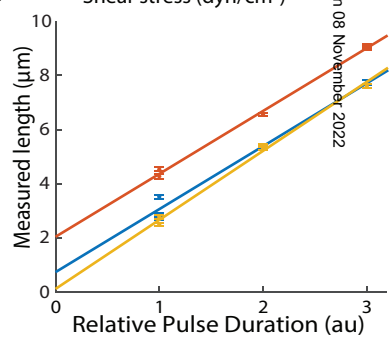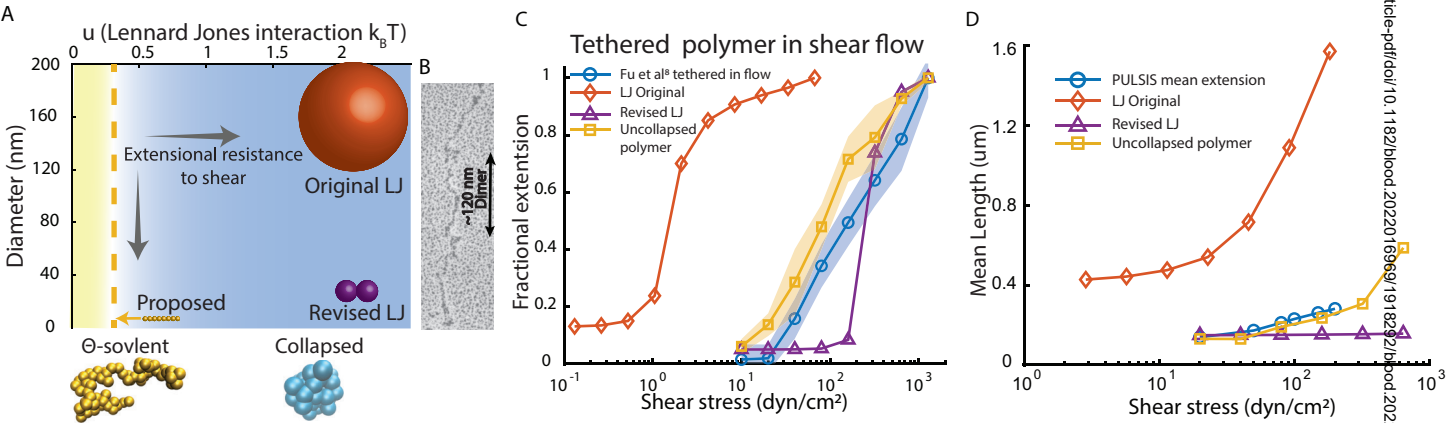
Figure 1.

Figure 2.

Figure 3.
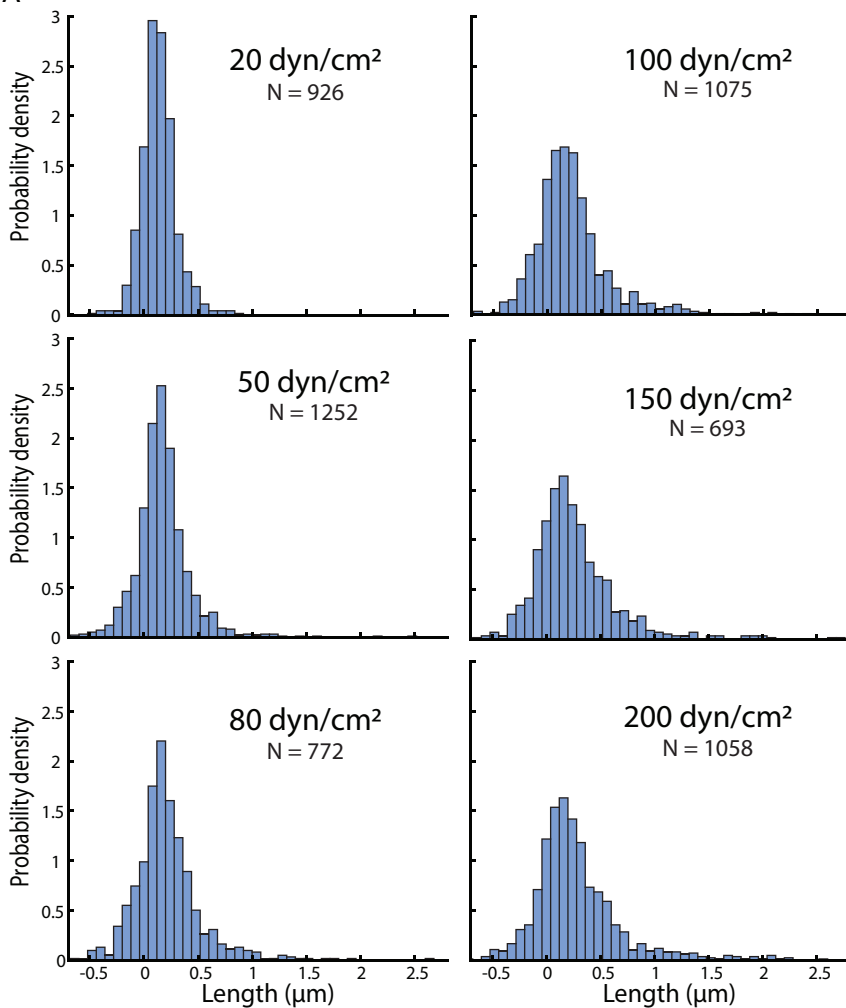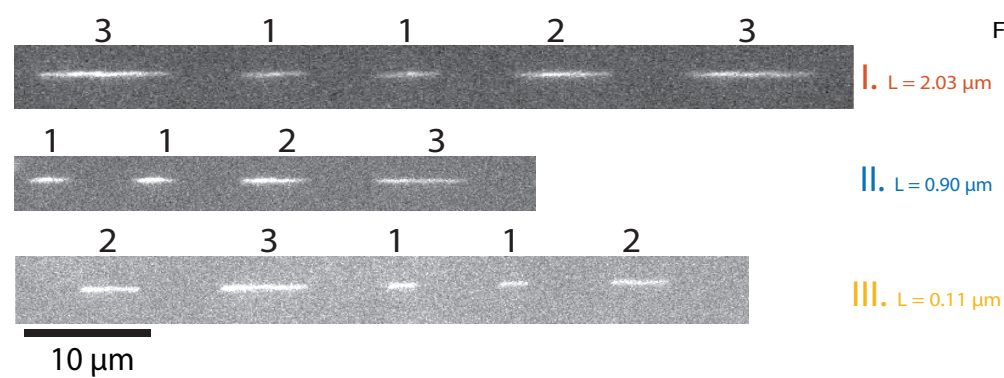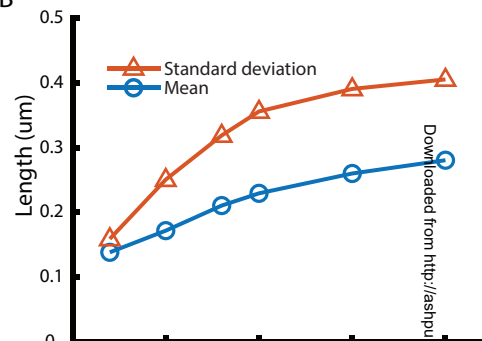
Figure 4.

1 Detailed methods

1.1 VWF and control preparation

Recombinant, therapeutic human VWF was labeled with Alexa Fluro 488 and biotin through non-specific NHS-ester lysine labeling and purified through size-exclusion chromatography as described by Fu et al.[1] The biotin was used for attachment to the surface for extension measurements, which were used to test for viscosity dependence and estimate length distribution. For the positive control, M13mp18 RF I DNA (N4018S NEB, Ipswich, MA) was used as the DNA control. The plasmid was linearized with SfoI restriction enzyme (R0606S NEB) at a final concentration of 385 units/ml with 20 ng/ ul m13 DNA in 1x NEB cut smart buffer. The reaction was incubated for 37°C for one hour and heat inactivated at 80°C for 20 minutes. Plasmid linearization was confirmed by a shift on an agarose gel. DNA was diluted to 5 ng/µl (7.6 µM base pair) in 20 mM Tris-HCL (pH 8.0). YOYO-1 dye was diluted to 1.9 µM in an equal volume of water. An equal volume of dye solution was added to DNA and incubated for 2 hours at 50 degrees Celsius for 2 hours. Labeling was confirmed visually on a fluorescent microscope. DNA imaged at 0.001 ng/µl along with 40% sucrose, 20 mM HEPES (N-2-hydroxyethylpiperazine-N'-2-ethanesulfonic acid pH 7.4), 0.02% Tween-20, 0.5 mg/ml BSA together with 2.2 mM protocatechuic acid (Santa Cruz Biotechnology, Santa Cruz, CA, USA) and 37 nM protocatechuate-3,4-dioxygenase (Sigma-Aldrich) as oxygen scavengers. For the negative control, fluorescent beads (F8803 Thermo Fisher Scientific yellow/green FluoSpheres Waltham, MA) with a diameter of 0.11 µm as determined by the manufacturer were used. They were imaged in 60% (w/w) sucrose with 20 mM HEPES (pH 7.4), 150 mM NaCl, 0.02% Tween 20 and 0.5 mg/ml BSA.

1.2 Flow application and Microscope

A home built TIRF microscope with a 485 nm laser (CUBE 485-30C, Coherent, Santa Clara, CA, USA), 60× oil TIRF objective (NA 1.49, CFI Apo TIRF 60× H, Nikon, Japan) and an EMCCD camera (DU-897, Andor, UK) was used. The flow is applied through a pressure difference between atmosphere and a high-pressure reservoir controlled by an electronic pressure regulator. Image acquisition and flow was controlled through custom built software (Labview) and laser pulsing was controlled independently with an arbitrary waveform generator (Hewlett Packard 33120A, Palo Alto, Ca). The flow chip was made by cutting 0.5 mm× 15 mm channels in double sided Kapton tape (100 µm thick) and sandwiching between a 1.5 low-density biotin-PEG/PEG-coated 1.5 cover glass (Bio 01, MicroSurfaces, Englewood, NJ) and 1.1 mm thick glass slide with holes drilled to insert flow tubing. A polydimethylsiloxane slab with holes stacked on top of the glass slide and the whole chip is clamped between a custom-made metal holder and plastic

cover with screws.

1.3 Pulsed Laser Stroboscopic Imaging of Single molecules (PULSIS)

Channels were initially blocked with BSA (BSA-Block, Candor, Germany) for 1 hour at room temperature and then washed 3x with 150 ul of PBS. Unless otherwise noted, the imaging buffer used was 60% sucrose, 150 mM NaCl, 20 mM HEPES (pH 7.4), 0.02% Tween 20, 0.5 mg/ml BSA together with 2.2 mM protocatechuic acid (Santa Cruz Biotechnology, Santa Cruz, CA, USA) and 37 nM protocatechuate-3,4-dioxygenase (Sigma-Aldrich) as oxygen scavengers. VWF was imaged at a concentration of 1.4 nM. The buffer was flown onto the chip. For the negative control, data was taken at 20, 50, 100 and 200 dyn/cm^2. The positive DNA control was imaged at 20 dyn/cm2 for both circular and linearized forms. VWF was imaged at 6 20, 50,80, 100,150 and 200 dyn/cm^2. The given shear stress was applied, and the molecules were imaged as follows. The laser pulses are generated with an arbitrary waveform generator (HP 33120A) with the laser pattern of 1 on, 3 off, 1 on, 3 off, 2 on, 3 off, 3 on, 3 off. Because we are interested in the of a zero duration pulse at the y-intercept, the actual duration of the pulses is not important as long as the relative duration is maintained. The frequency of the pulse cycle was tuned such that at least one full cycle was completed within the exposure time with a single pulse unit between 2-20 ms. The exposure time was set so that a particle would travel around half a field of view within the exposure. This increased the likelihood of capturing a full pulse sequence. Both frequency and exposure were changed to match the shear, with higher shear stresses having higher frequencies and lower exposure time. The molecules were imaged in a quasi-TIRF mode with particles roughly 3 µm above the surface. The molecules were flown in a single direction to avoid photobleaching. Based on an angular velocity of $\frac{1}{2}$ the shear rate [2], the shortest pulse was approximately the time for 0.1 rotations of the molecule. Molecules were imaged for 200 frames at a time.

1.4 Image Analysis

PULSIS trajectories were analyzed with custom MATLAB scripts. Trajectories were manually selected and the intensity profile along the direction of flow was calculated. A hidden Markov model, with manual oversight, was used to roughly find each individual laser pulse. The molecules are assumed to have a uniform, 2D gaussian point spread function which moves through time given as

$$I\left(x, y, t\right) = \frac{1}{\sigma\sqrt{2\pi}} e^{-\frac{(x-vt)^2}{2\sigma^2}} e^{-\frac{(y)^2}{2\sigma^2}} \tag{1}$$

For each individual pulse, the intensity profile along perpendicular to the flow is found. The profile

2

is fit to a 1D gaussian and standard deviation taken as the width of the point spread function for both directions. Next, the intensity profile is found in the direction of flow. The background is subtracted based on the average intensity profile on either side of the pulse. The camera image is analogous to integrating the 2D gaussian function over some time (from t1 to t2). The intensity profile should be equivalent to further integrating the function along the y direction. This gives

$$Ip\left(x\right) = N\left(-Erf\left[\frac{d1-x}{\sqrt{2}\sigma}\right] + Erf\left[\frac{d2-x}{\sqrt{2}\sigma}\right]\right) \tag{2}$$

The value is found from the previous fit of the intensity profile in the perpendicular direction. The N represents a normalization factor which has no impact on the measured length. The values of t1 and t2, multiplied by a constant velocity give two distances d1 and d2, which represent the location of the center of the fluorescent particle at the start and end of the time interval. The intensity profile is fit to this function. The length of the pulse is the difference between the fitted values d2 and d1. The error for each pulse is based on the diagonal components of the covariance matrix for the estimated coefficients d1 and d2. After the length of each pulse in the trajectory is found, the pulse duration (1,2,3) is assigned based on the pulse pattern and length. A linear regression, with the fitting errors, is preformed based on the pulses and duration according to the methods of York et al.[3]. The y-intercept is used as the true length of the molecule. Linear regressions were further filtered based on the r2 value, with trajectories where $r^2 < 0.95$ are discarded.

1.5   Relaxation conformation

The lengths and fluorescence profiles in the direction of flow were obtained from Fu et al. [1]. The molecules are extended at high shear (1280 dyn/cm2) for five frames and the flow is turned off. The relaxation conformation was calculated as follows, with visual demonstration in supplemental figure 8. The fluorescence intensity was integrated from the tether point to the end to find the total fluorescence intensity. The integrated intensity at half the length was found, with the exact value found with linear interpolation. A fractional threshold is found by taking the integrated intensity at half-length to the total integrated intensity for each frame at high shear and averaged. This fractional threshold is found to take into account the initial non-uniform distribution. Once the flow is turned off, the total integrated intensity is found again for each frame. The length required to reach the initial fractional fluorescence is found. This length is divided by the total extension for that frame to get a fractional extension. The fractional extension F is divided by 1-F to give a ratio of the lengths containing the same fractional fluorescence that initially was in each half. The values are binned based on the fractional extension. The simulation is processed in an analogous way, with the full trajectories being used to make a fluorescence distribution. Kymographs for simulations were

3

created to closely match experimental conditions, taking into account exposure time, time between frames, and pixel size along with a 2D gaussian image filter to approximate a point spread function (supplemental figure 6B-D,9).

1.6   Experimental steady-state stretching of surface-tethered VWF

Steady-state stretching of surface-tethered VWF followed the procedure given by Fu et al [1]. The channel was blocked with a mixture of BSA and casein for 1 hour at room temperature. Traptavidin (0.1 µg ml^{-1}) (Kerafast, Boston, MA, USA) was added to the channel and allowed to incubate approximately 10 minutes. The Traptavidin was washed away with 3x washes of PBS. VWF at 80 nM was incubated in the chamber until the correct density of surface-tethered VWF was achieved ($\approx$ 10 min) as determined by visual inspection. Afterwards, excess VWF was washed from the chamber and the chamber was blocked with 5 mM D-biotin for an additional 10 minutes. The biotin was washed away gently with 1x wash of PBS and buffer containing 150 mM NaCl, 20 mM HEPES (pH 7.4), 0.02% Tween 20, 0.1 mm biotin, 0.5 mg/ml BSA together with 2.2 mM protocatechuic acid (Santa Cruz Biotechnology, Santa Cruz, CA, USA) and 37 nM protocatechuate-3,4-dioxygenase (Sigma-Aldrich) was flowed in. VWF length extension was measured at 8 different shear rates, in both directions. At a given shear rate, flow was turned on and the VWF molecules were imaged for 5 frames at 0.3 frames/sec, flow was then stopped for 5 frame, and then the flow was applied in the opposite direction for an additional 5 frames. The shear rates measured were 10, 20, 40, 80, 160, 320, 640, and 1280 dyn/cm^2. After measuring a single field of view, the aqueous buffer was flowed out of the chamber and replaced with the equivalent buffer in 60% w/w sucrose. The flow extension in the same field of view was again measured in both directions in the viscous buffer at the equivalent 8 shears stresses. The viscous buffer was flowed out and replaced with aqueous buffer and then VWF extension was remeasured to ensure that there was no hysteresis effects.

2   Simulations details

2.1   Description

VWF was modeled as chain of spherical beads. The polymer was simulated with a Brownian dynamics simulations where the bead positions were updated based on numerical integration of the following discretized Langevin equation [4][5][6][7]

$$r_i(t + \Delta t) = r_i(t) + \left(\dot{\gamma} z_i \mu_0^{-1} \mu_{ii} \cdot \hat{x} + k_B T \frac{d\mu_{ii}^{zz}}{dz} \hat{z} - \sum_{j=1}^{N} \mu_{ij} \cdot \left(\nabla_{r_{ij}} U_m(t) + \nabla_i U_w(t) \right) + \xi_i(t) \right) \Delta t \qquad (3)$$

Here, $r_i(t)$ represents the position of bead i at time t and $r_i(t + \Delta t)$ is the position of bead i at the next time step. The simulation is given a time step $\Delta t = 2 * 10^{-4} \tau$, with τ being the characteristic bead diffusion time $\tau = \frac{6\pi\eta a^3}{k_B T}$ (η is the viscosity, a is the bead radius, k_B is the Boltzmann Constant and T is temperature).

The first term, $\dot{\gamma} z_i \mu_0^{-1} \mu_{ii} \cdot \hat{x}$, accounts for the velocity due to the shear flow and is dependent on the specified shear rate $\dot{\gamma}$, the bead height above the surface z_i, the inverse of the Stokes mobility of a sphere μ_0, and the corresponding component of the hydrodynamic mobility tensor μ_{ii}. The velocity is in the direction of flow ($\hat{x}$). The stokes mobility of a sphere is defined as $\mu_0 = \frac{1}{6\pi\eta a}$.

The last term, $\xi_i(t)$, represents the random velocities from the Brownian motion, which satisfies the fluctuation dissipation theorem

$$\langle \xi_i(t) \xi_j(t') \rangle = 2 k_B T \mu_{ij} \delta(t - t') \qquad (4)$$

The mobility matrix μ_{ij} accounts for the hydrodynamic interactions between the ith and j^{th} bead. For all surface tethered molecules, the hydrodynamic interaction is approximated as the Rotne-Prager-Blake tensor which accurately describes both the hydrodynamic interactions between beads and the surface [8][9]. The explicit terms of the mobility tensor can be found in Von Hansen et al.[10]. For the non-tethered cases, the Rotne-Prager-Yamakawa tensor was used for the mobility matrix which can be found explicitly written in Wajnryb et al. [11]. The hydrodynamic tensor was updated every 100 time steps.

$k_B T \frac{d\mu_{ii}^{zz}}{dz}$ is a correction for the divergence of the diffusion tensor resulting from the no-slip condition at the surface and is defined as [10]

$$k_B T \frac{d\mu_{ii}^{zz}}{dz} = \mu_0 \left(\frac{9a}{8z_i^2} - \frac{3a^3}{2z_i^4} \right) \qquad (5)$$

Here, z_i is defined as the height of the ith bead above the surface, a is the radius of a bead, and μ_0 is the mobility of a sphere. This term is not included in the case where the surface is absent.

The potential energy of each bead is based on two terms, $U_w(z_i(t))$ and $U_m(t)$. The first term, U_w, is the hard core repulsion due to the wall based on the height from the surface z of the ith bead at time t. This potential is not included in the case where the surface is absent. At a given time, this is specified as [7]

$$U_w(z_i) = \begin{cases} 2\pi k_B T 1.5a(4/(5z_i))^{10} - (3/(2z_i)^4 + (3/5)) & \text{if } z_i < 1.5a \\ 0 & \text{if } z_i > 1.5a \end{cases} \tag{6}$$

The potential energy term $U_m(t)$ defines the interaction potential between monomers. The potential is based on non-specific a Lennard-Jones interaction between all beads and a FENE potential connecting adjacent beads.

$$U_m = U_{LJ} + U_{fene} \tag{7}$$

The first potential U_{LJ} is the Lennard-Jones term which applies a non specific potential between all beads defined as

$$U_{lj}(r_{ij}) = u_{LJ} \left[(\frac{2a}{r_{ij}})^{12} - 2(\frac{2a}{r_{ij}})^6 \right] \tag{8}$$

Here, r_{ij} is the distance between bead i and j, a is the bead radius, and u_{LJ} is the interaction strength. The potential is set to zero for any beads farther than $24a$ apart. For the Lennard-Jones model, the interaction parameter is set to $u_{LJ} = 2.08k_BT$, with a radius of a = 80 nm. For the revised model, the interaction strength was also set to $u_{LJ} = 2.08k_BT$ based on matching experimental data for the shear stress required for half extension given a bead radius of a = 14 nm. For the uncollapsed polymer, this is set to the Θ-point $u_{LJ} = 0.314k_BT$, where the beads neither repel nor attract each other with the bead radius set to a = 3.7 nm.

To keep successive monomers together, a finitely extensible nonlinear elastic model or FENE potential U_{FENE} was used. Due to the high flow used, the FENE spring constant is set at $H_{FENE} = 800 \ k_B T/a^2$ and a maximum bond length of $Q_{max} = 1.5 * 2 * a \frac{1}{2^6}$ [12]

$$U_{FENE} = \frac{-1}{2} H_{FENE} Q_{max}^2 \sum_i^{N-1} Log \left[1 - (\frac{r_{i,i+1} - 2a}{Q_{max}})^2 \right] \tag{9}$$

The first bead is tethered to the surface by a FENE bond with its center point 2a above the surface.

The parameters parameters that distinguish each model are as follows

Table 1: Parameters for Models

Model	bead radius (nm)	Lennard-Jones interaction $u_{LJ}(k_BT)$
Original LJ model	80	2.08
Revised LJ model	14	2.08
Uncollapsed polymer	3.7	0.314

2.2 Setup

Equilibration times and number of trials were determined by variation between trials, time to convergence and computational time.

2.2.1 Relaxation

For each model type, the model was initialized as a linear chain space 2a from the surface, with a being the bead radius with one end attached to the surface. The chains were allowed to relax with no flow for 125,000*N time steps, with N being the number of beads in the chain. The length of the time step is defined above. High shear flow (1280 dyn/cm^2) was applied for another 125,000*N time steps after which the flow was turned off to simulate the relaxation of a molecule. The bead positions were saved every 5000 time steps. Ten simulations were done for each model and bead number and averaged at each time point. The final positions were saved and used as an initial conformation for the subsequent simulations.

2.2.2 Surface tethered Equilibration

Polymers were attached on one end to a surface and shear flow was applied. For each model type, the model was initialized based on the final bead positions for the relaxation study, with the first bead tethered to the surface at a height 2a from the surface. The simulations were allowed to relax for an additional time with no flow, with the times in the tables below. After which flow was applied and allowed to equilibrate before measuring the extension. The equilibration and measuring times are given below in terms of time steps. For each condition, five trials were simulated. The extension for each simulation was averaged over the windows detailed in table 2-4, and the mean extension of each trial were further averaged and plotted. Duration is given in units of the time step Δt.

Table 2: Original LJ model Equilibration

Beads	Equilibration time with flow	Measuring Window (duration)
10	$1.13 * 10^7$	$1.8 * 10^6$
20	$2.25 * 10^7$	$3.75 * 10^6$
30	$3.38 * 10^5$	$5.63 * 10^6$
40	$4.5 * 10^5$	$7.5 * 10^6$

Table 3: Revised LJ model Equilibration

Beads	Equilibration time with flow	Measuring Window (duration)
50	$2.19 * 10^7$	$3.13 * 10^6$
100	$4.38 * 10^7$	$6.25 * 10^6$
150	$6.56 * 10^7$	$9.38 * 10^6$
200	$8.75 * 10^7$	$1.25 * 10^7$

Table 4: Uncollapsed polymer model Equilibration

Beads	Equilibration time with flow	Measuring Window (duration)
200	$2.0 * 10^7$	$5.0 * 10^6$
300	$2.5 * 10^7$	$7.5 * 10^6$
400	$7.0 * 10^7$	$1.0 * 10^7$

2.2.3 Free VWF in shear

For each model type, the model was initialized based on the final relaxation bead positions, with all surface interactions removed. The model was allowed to relax for 375,000*N time steps where N is the total number of beads in the simulation. For the LJ models, extension was recorded every 500 time steps. For the uncollapsed polymer, extension was recorded every 1000 time steps. Simulations averaged over measuring window and trials. Duration is given in units of the time step Δt.

Table 5: Original LJ model free in flow

Beads	Equilibration time with flow	Measuring Window (duration)	Trials
50	$3.75 * 10^6$	$3.13 * 10^7$	3
100	$7.5 * 10^6$	$6.25 * 10^7$	3
150	$1.13 * 10^7$	$5.0 * 10^7$	3
200	$1.5 * 10^7$	$3.2 * 10^7$	3

Table 6: Revised LJ model free in flow

Beads	Equilibration time with flow	Measuring Window (duration)	Trials
50	$1.8 * 10^7$	$1.5 * 10^8$	3
100	$3.75 * 10^7$	$3.13 * 10^8$	3
150	$5.6 * 10^7$	$3.13 * 10^8$	3
200	$7.5 * 10^7$	$1.5 * 10^8$	3

Table 7: Uncollapsed polymer model free in flow

Beads	Equilibration time with flow	Measuring Window (duration)	Trials
200	$2.0 * 10^6$	$2.0 * 10^8$	10
300	$1.0 * 10^7$	$1.0 * 10^8$	10
400	$2.0 * 10^7$	$1.9 * 10^8$	10

3   Problems with Fiducial beads for motion blur correction

Correcting for motion blur is essential for measuring VWF extension in shear flow. One approach adds fiduciary beads to subtract out the motion [13]. Due to the linear relationship between surface height and velocity in pure shear flow, fiducial beads can only correct for motion blur if the relative surface height between a bead and a VWF molecule are precisely known. VWF imaged at high shear rates of 5000 s^{-1} (50

dyn/cm^2) with a frame rate of 25 frames per second and focus set 5 µm above the surface would be moving at 1000 $\mu m/frame$. A surface height error of only 70 nm could lead to apparent length differences of 14 µm/frame (ΔSurface Height $*$ shear rate/frame rate), similar to the length they claim for VWF molecules extended by flow. Yet even a high numerical aperture microscope objective (e.g., 1.4) only has an axial resolution of approximately 500 nm, as determined by the Abbe diffraction limit. Consequently, the error introduced by this type of motion blur correction would likely be larger than the signal.

4   Tension estimation

To estimate the tension in the polymer, we used the concept of an entropic spring. A chain of beads will have an equilibrium end-to-end extension and a force is required to perturb the mean extension away from this point. The mean extension can be used as a proxy for force. We calibrated the spring by having a polymer of 10 beads with one end tethered to a point. A constant force was applied in the direction of a vector pointing from the first bead to the last bead. The mean extension was found as a function of the applied force, giving a force-calibration curve that can translate an average extension of a 10 bead chain to an applied force, which we take as the tension (supplemental figure 5A). Using the force-calibration curve, the trajectories for the uncollapsed polymer were analyzed by segmenting them into 10-bead chains and looking at the mean extension of each segment as a function of shear. The extension was converted into a force based on the calibration curve and plotted (supplemental figure 5B). The spread of the force distribution was estimated by looking at distribution of the 10-bead segments. The dotted lines represent the 16th and 84th percentiles of extension of the forty 10-bead segments (400 bead polymer) converted into force with the calibration curve. The force value is only meaningful for the average extension and is not representative of force fluctuations, which could be higher. However, the average force for the polymer simulations is low, not exceeding 0.1 pN at physiological shear rates.

5   Polymer simulations for VWF relaxation

In addition to surface elongation of VWF under flow, we also simulate a surface tethered polymer relaxing from an extended state and compared to single molecule VWF data [1]. The relaxation gives information about the time scale of the polymer. Furthermore, the collapsed vs uncollapsed polymer models give distinct predictions of the molecule conformation that can be tested.

Briefly, VWF in a high-viscosity sucrose buffer is hydrodynamically stretched into an extended state by a high shear stress of 1280 dyn/cm^2. The shear flow is reduced to 0 dyn/cm^2 and the molecule length

is recorded as a function of time as the molecules collapse back down to a compact object. In our polymer models, the time scale of relaxation is largely influenced by the bead size as the larger beads diffuse slower and have lower mobility but must still collapse over the same absolute distance. The original LJ model, with the large bead radius, decays 20 times too slowly (supplemental figure 6A, 7A-C) . With a smaller bead radius and attractive potential, the revised LJ model decays on the correct times scale for lengths in the range of interest, as does the uncollapsed polymer model with the smallest bead radius. The relaxation times for all models fail to scale correctly as a function of length (supplementary figure 6D) indicating further room for improvement.

From the relaxation data, we can also extract information on the conformation of the molecule during collapse by looking at the distribution of fluorescence in the single molecule data. A collapsed polymer follows a ball and stem collapse where a ball forms at the end and moves toward the tether point, "eating" up the other beads [14] (supplemental 7C). In contrast, the uncollapsed polymer model shows more uniform collapse, like a rubber band. If a strong, non-specific interaction exists with VWF, the experimentally observed relaxation profile should indicate a ball at the free end that grows and gets brighter as the polymer collapses.

To investigate the shape, we use fluorescence as a proxy for polymer shape and look to see if fluorescence becomes concentrated at the free end as VWF relaxes. The fluorescence distribution ratio quantifies how the fluorescence changes(supplemental figure 8). We first find the total intensity in the first and second halves of the molecule when it is in the extended state and use this to define a fractional threshold. The fractional cumulative intensity at half the length gives an intensity threshold T which represents the initially fluorescence distribution between the first and second halves of the molecule. During each frame in the collapse, the intensity is integrated over the length until the fractional threshold T is reached. The fractional integration length L, relative to 1-L, roughly quantifies the fluorescence distribution shift at different time points, which we define as the fluorescence distribution ratio (FDR). This ratio is plotted as a function of fractional extension to remove any explicit time dependence (supplemental 6D,9A-D). The experimental data gives a value of 1 throughout the collapse, meaning the fluorescence distribution between the first and second halves remains constant throughout the molecule relaxation. For the 3 μm length molecues, both LJ models show an increase in this ratio as the molecule collapses, with the revised LJ model reaching up to 8. The uncollapsed polymer reaches a maximum value < 2, consistent with the observed VWF collapse. The uncollapsed polymer model is able to match both the timescale and relaxation conformation of VWF.

References

[1] Hongxia Fu, Yan Jiang, Darren Yang, Friedrich Scheiflinger, Wesley P. Wong, and Timothy A. Springer. Flow-induced elongation of von Willebrand factor precedes tension-dependent activation. *Nature Communications*, 8(1), 2017.

[2] A. Alexander-Katz and R. R. Netz. Dynamics and instabilities of collapsed polymers in shear flow. *Macromolecules*, 41(9):3363–3374, 2008.

[3] Derek York, Norman M. Evensen, Margarita López Martınez, and Jonás De Basabe Delgado. Unified equations for the slope, intercept, and standard errors of the best straight line. *American Journal of Physics*, 72(3):367–375, 2004.

[4] A. Alexander-Katz, M. F. Schneider, S. W. Schneider, A. Wixforth, and R. R. Netz. Shear-flow-induced unfolding of polymeric globules. *Physical Review Letters*, 97(13):1–4, 2006.

[5] Richard Schwarzl and Roland R. Netz. Hydrodynamic shear effects on grafted and non-grafted collapsed polymers. *Polymers*, 10(8):27–30, 2018.

[6] Donald L. Ermak and J. A. McCammon. Brownian dynamics with hydrodynamic interactions. *The Journal of Chemical Physics*, 69(4):1352–1360, 1978.

[7] Matthias Radtke, M. Radtke, and R. Netz. Shear-induced dynamics of polymeric globules at adsorbing homogeneous and inhomogeneous surfaces. *European Physical Journal E*, 37(3), 2014.

[8] Charles E. Sing, Jennifer G. Selvidge, and Alfredo Alexander-Katz. Von Willlebrand adhesion to surfaces at high shear rates is controlled by long-lived bonds. *Biophysical Journal*, 105(6):1475–1481, 2013.

[9] Nazish Hoda and Satish Kumar. Polyelectrolyte adsorption in shear flow with hydrodynamic interaction: Kinetic theory and brownian dynamics simulations. *AIP Conference Proceedings*, 1027(2007):968–969, 2008.

[10] Yann Von Hansen, Michael Hinczewski, and Roland R. Netz. Hydrodynamic screening near planar boundaries: Effects on semiflexible polymer dynamics. *Journal of Chemical Physics*, 134(23):1–15, 2011.

[11] Eligiusz Wajnryb, Krzysztof A. Mizerski, Pawel J. Zuk, and Piotr Szymczak. Generalization of the Rotne-Prager-Yamakawa mobility and shear disturbance tensors. *Journal of Fluid Mechanics*, 731, 2013.

[12] Kurt Kremer and Gary S. Grest. Dynamics of entangled linear polymer melts: A molecular-dynamics simulation. *The Journal of Chemical Physics*, 92(8):5057–5086, 1990.

[13] S. W. Schneider, S. Nuschele, A. Wixforth, C. Gorzelanny, A. Alexander-Katz, R. R. Netz, and M. F. Schneider. Shear-induced unfolding triggers adhesion of von Willebrand factor fibers. *Proceedings of the National Academy of Sciences*, 104(19):7899–7903, 2007.

[14] Axel Buguin and Françoise Brochard-Wyart. Unwinding of globular polymers under strong flows. *Macromolecules*, 29(14):4937–4943, 1996.
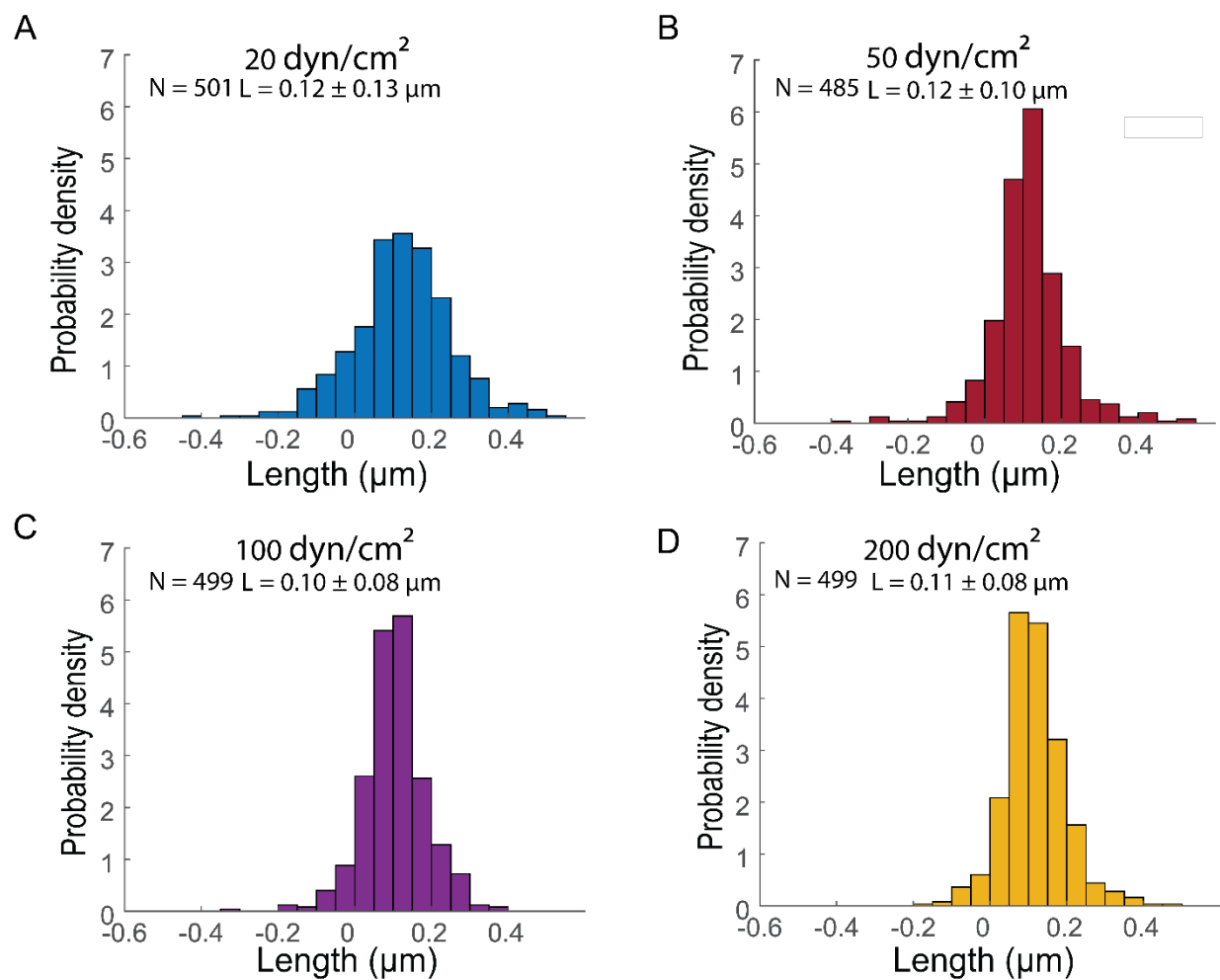
Supplemental Figure 1. Raw histograms of bead length from fig 2F. Negative control for PULSIS validation, imaging 110 nm fluorescent beads 20 (**A**), 50 (**B**), 100 (**C**), and 200 (**D**) dyn/cm². Number of measurements (N) and mean length (L) ± standard deviation for each condition is shown.
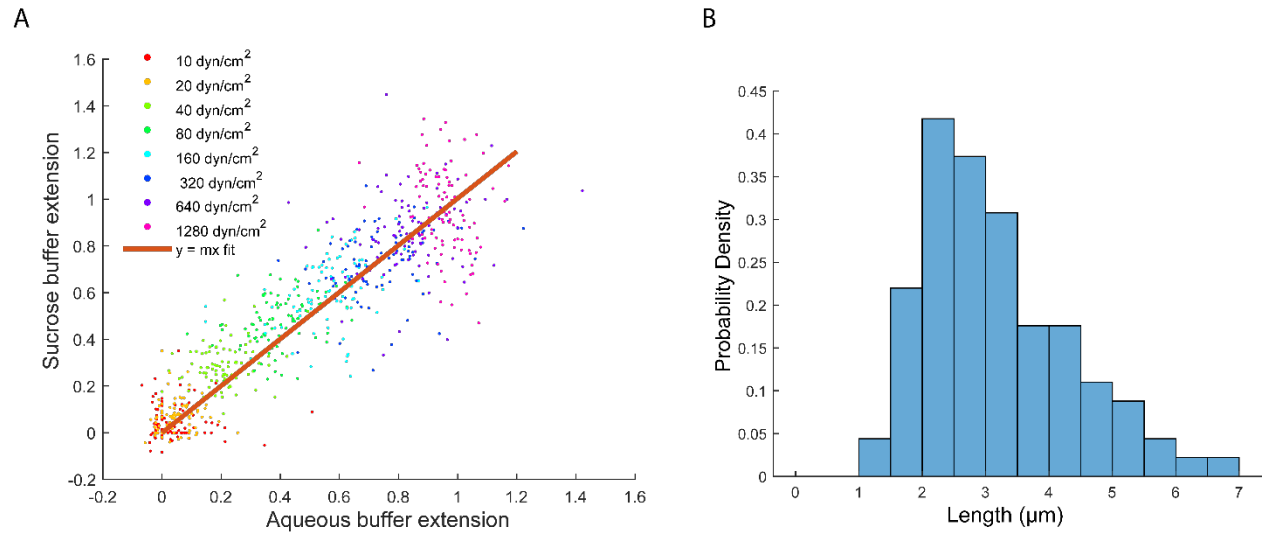
Supplemental Figure 2. VWF surface extension in non-viscous and viscous buffers. A. Molecules were attached to the surface through biotin-traptavidin, shear stress was applied and the molecule length was measured. Each dot represents the normalized extension of a single molecule at a specific shear (specified by color) in a single direction measured in both aqueous (x coordinate) and sucrose (60% w/w) buffer (y coordinate). The slope is a linear regression with the y-intercept fixed to zero, giving a slope of m = 1.004. All molecules are normalized by the average of the forward and reverse flow length measurements at 1280 dyn/cm^2 in aqueous buffer. Overall, there are 1456 measurements, which breaks down to 91 molecules at 8 shears in 2 directions (91*2*8). **B**. Length distribution of VWF at highest shear stress (1280 dyn/cm^2) in aqueous buffer. N= 91, mean = 3.1 μm.
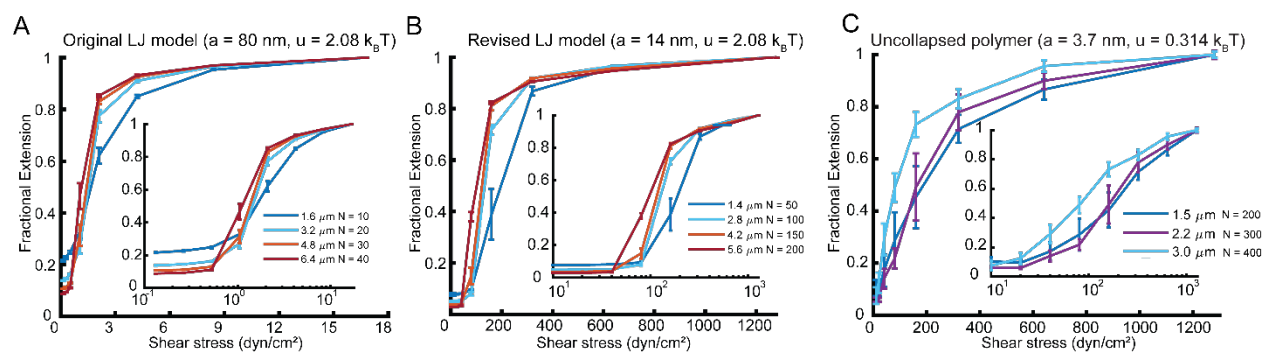
Supplemental Figure 3. Simulation of surface tethered polymer in shear flow for different models with expanded lengths. Polymers have one end attached to the surface, allowed to relax with no flow and then shear flow is applied. For each model, five simulations are run at each shear. Fractional extension is calculated based on the average extension of the five trials at the highest shear stress. Error bars are based off of the standard deviation of the five trial lengths at each shear stress. The three models are the original LJ model (**A**), the revised LJ model (**B**), and the uncollapsed polymer model (**C**). Inset is data replotted on a semi-log x plot. Estimated lengths in the legend are based on contour length, N represents the number of beads in the simulation, a is the radius of a bead for that model type, and u is the Lennard Jones potential interaction constant of that model. Due to the large number of beads and the resulting long computational time for the uncollapsed polymer, only a chain up to ~3 μm (N = 400) was simulated. Number of simulations, equilibration, time averaged over etc. in supplemental text 2.2.2
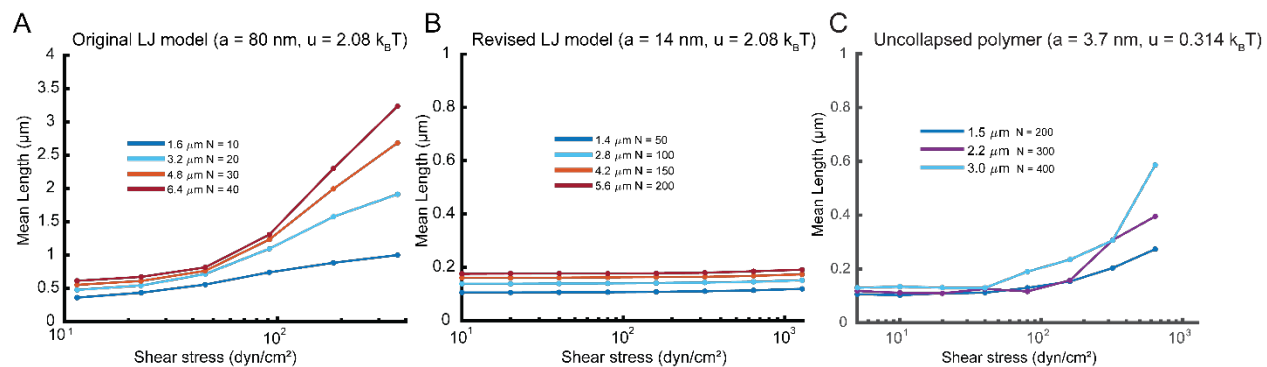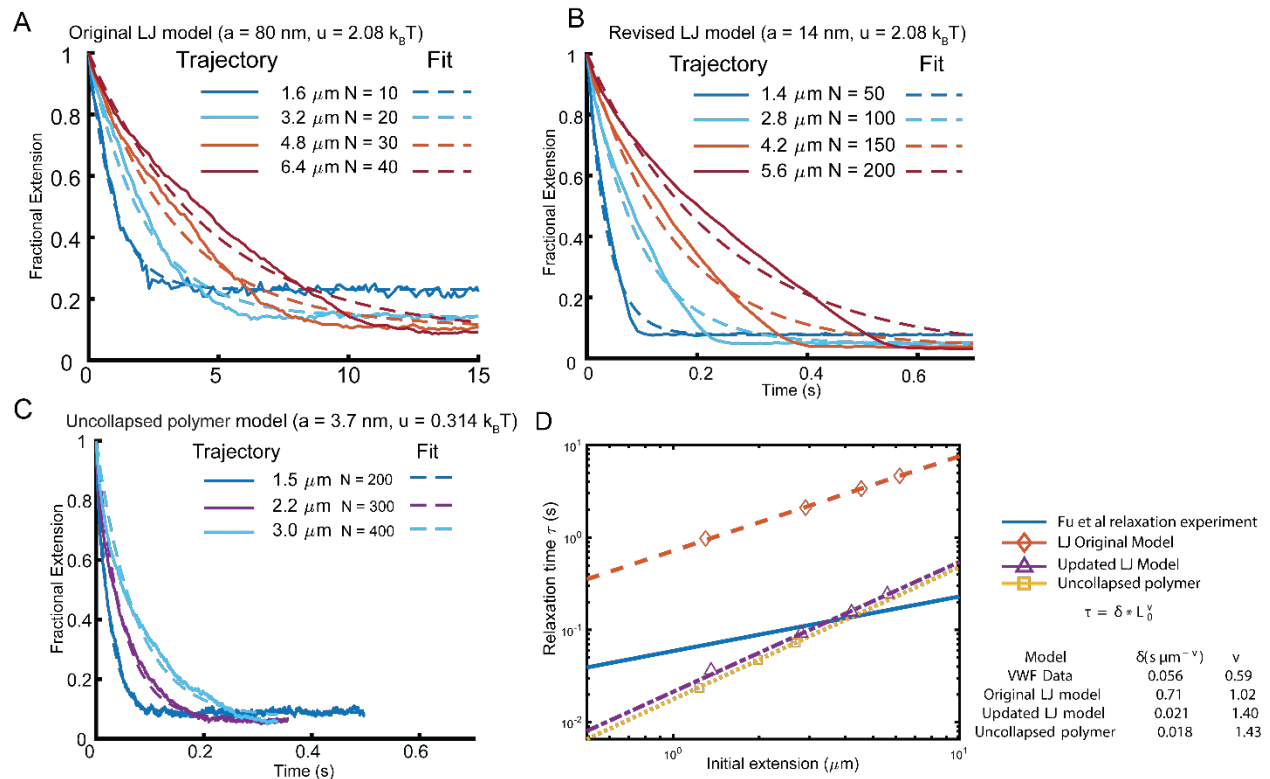
Supplemental Figure 4. Simulation of a free polymer in shear flow for different models with expanded lengths. Polymers are allowed to equilibrate under no flow. After, shear flow is applied, the extension is recorded, and the mean extension is plotted. Extension is measured as the maximum distance between any two points of polymer along the flow axis. The three models are the original LJ model (**A**), the revised LJ model (**B**), and the uncollapsed polymer model (**C**). Estimated lengths in the legend are based on contour length, N represents the number of beads in the simulation, a is the radius of a bead for that model type, and u is the Lennard Jones potential interaction constant of that model. Due to the large number of beads and the resulting long computational time for the uncollapsed polymer, only a chain up to ~3 µm (N = 400) was simulated. Number of simulations, equilibration, time averaged over etc. in supplemental text 2.2.3
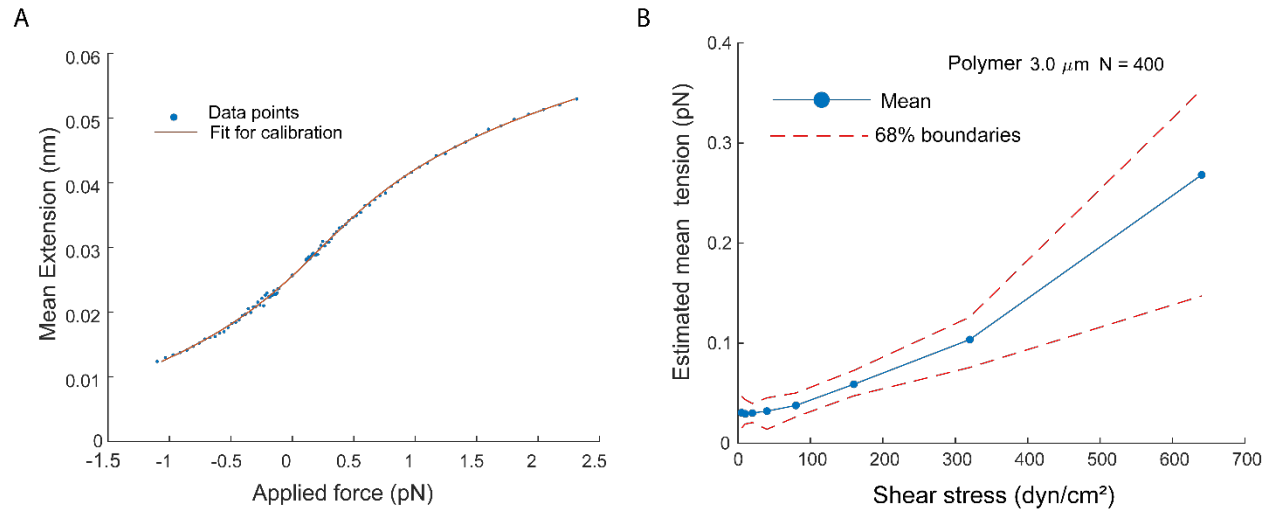
Supplemental Figure 5. Calculation of estimated tension for the free uncollapsed polymer model. To calculate the average tension along a simulated polymer, the polymer is analyzed as a collection of entropic springs in series, each with a defined length of 10 beads long, which is roughly the length of a single VWF monomer. For each entropic spring, a force-calibration curve is used to convert the average extension to the applied force, or tension, required to extend the spring to that distance, working against entropy. **A.** Spring force calibration. The spring was calibrated by determining the mean extension of a 10mer in the presence of a constant force, applied in the direction of the vector pointing from the first bead to the last bead. The force-calibration curve was then generated by fitting an arbitrary function to the simulated mean extension vs. force to allow for a conversion between 10mer extension and applied force. **B.** Mean tension of the uncollapsed polymer as a function of shear stress. For the trajectories in supplemental figure 4C, each polymer was segmented into 10mers, the average 10mer extension was calculated and the calibration curve was used to convert each extension to an applied force. In addition to mean tension vs. shear stress, boundaries are also presented (red dotted lines) based on the distribution of the mean extensions of each 10 chain segment within the polymer (40 total per 400 bead chain). Extensions of the 16th and 84th percentiles were converted to force based on the calibration curve and plotted with the dotted line. The mean tension was below 0.1 pN for physiological shear stresses (less than or equal to 80 dyn/cm^2).
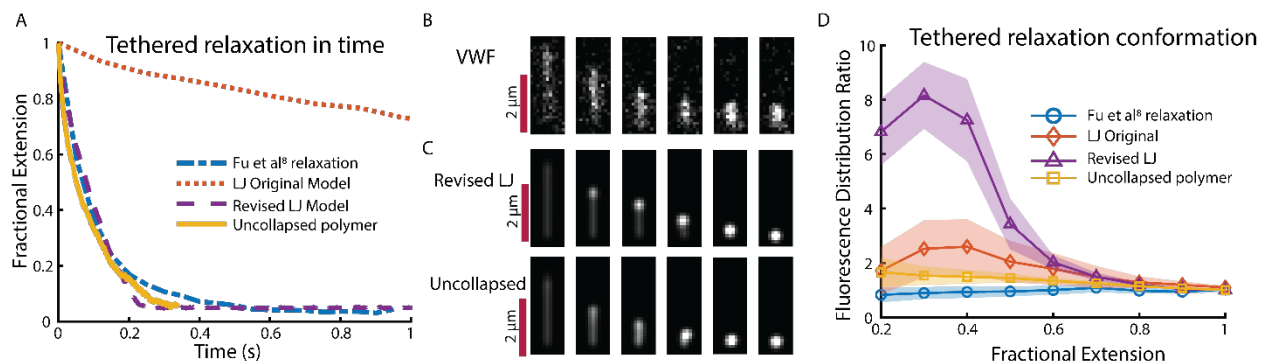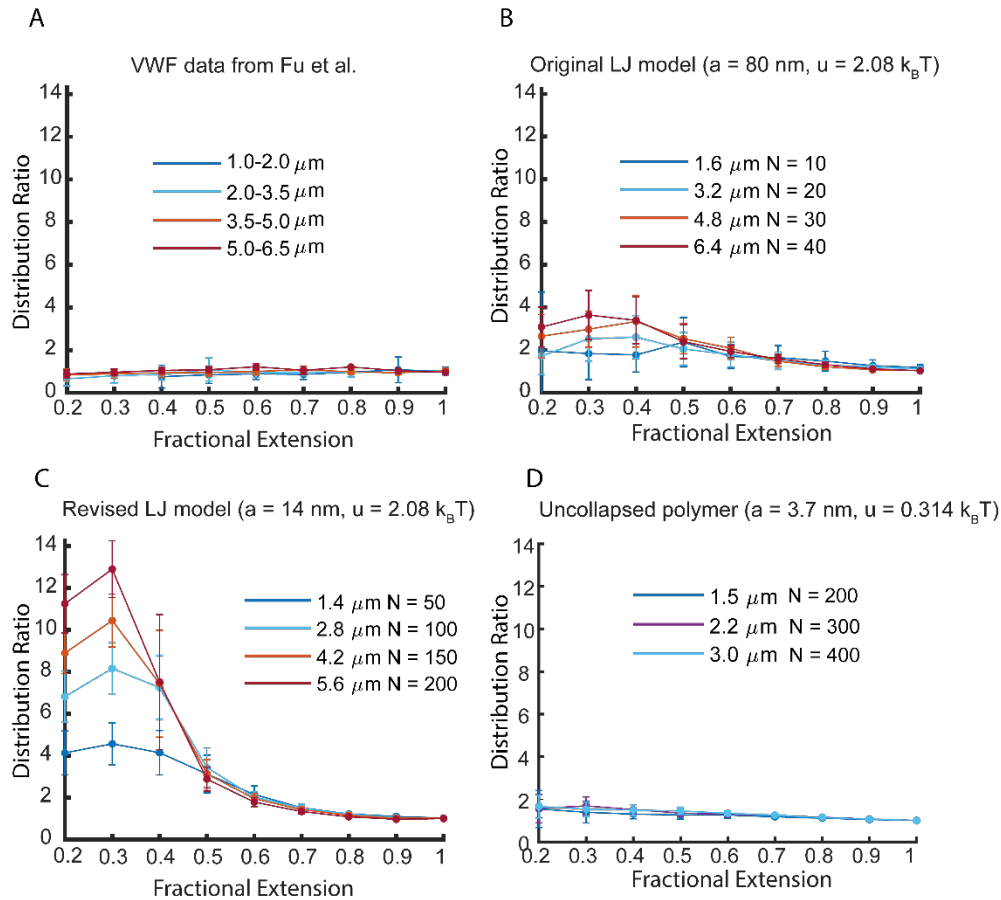
Supplemental Figure 6. Polymer relaxation comparison. A. Relaxation profiles for the three models compared to experimental VWF relaxation data. Polymers are based on a contour length of ~3 µm and data is for molecules with a maximum extension of 2.0-3.5 µm. For each condition, replicates where run and normalized extension was averaged at each point in time. **B.** Relaxation kymograph of VWF in in high viscosity buffer (58 centipoise) based on data from Fu et al[6]. VWF starts out as extended under shear with one end attached to the surface, shear is turned off and the polymers relax back down. **C.** Kymograph of relaxation for polymer simulations (revised LJ and uncollapsed polymer) highlighting relaxation conformation differences. **D.** Fluorescence distribution ratio (described in supplemental figure 8) plotted as a function of fractional extension for the different models compared to VWF data. Fluorescence distribution ratio is the required integration distance **Id** over 1 - **Id,** where **Id** is the distance to reach the initial normalized cumulative fractional fluorescence at half extension. Reports on conformation of collapse, rather than time scale. Shading represents one standard deviation. Simulations are from 10 independent trials. Data represents 156 molecules.

Supplemental Figure 7. Brownian dynamic simulation of an elongated, surface tethered polymer relaxing under no flow for different models with expanded lengths. Polymers are tethered to the surface and allowed to equilibrate with high shear flow. Once the flow is turned off, the extension in the direction that flow was applied is recorded as the molecules relax. For each model, ten simulations are run at each length and averaged together at each point in time. Relaxation decay is fit to a single exponential $L/L_0 = 1 - a + a * exp(-t/\tau)$, with the fit plotted as a dotted line. The three models are the original LJ model (**A**), the revised LJ model (**B**), and the uncollapsed polymer model (**C**). Estimated lengths in the legend are based on the contour length, N represents the number of beads in the simulation, a is the radius of a bead for that model type, and u is the Lennard Jones potential interaction constant of that model. Due to the large number of beads and the resulting long computational time for the uncollapsed polymer, only a chain up to ~3 μm (N = 400) was simulated. **D.** Relaxation time scaling as a function of initial extension. Relaxation times from the exponential fit are fit to $\tau = \delta * Lo^{v}$, with τ being the relaxation time and Lo is the initial length, with δ and v being free parameters. Fitted values are given in the table. Data from Fu et al.[2] is plotted for VWF. None of the models relaxation time scale similar to VWF as a function of initial length. Number of simulations, equilibration, time averaged over etc. in Supplemental Text 2.2.1
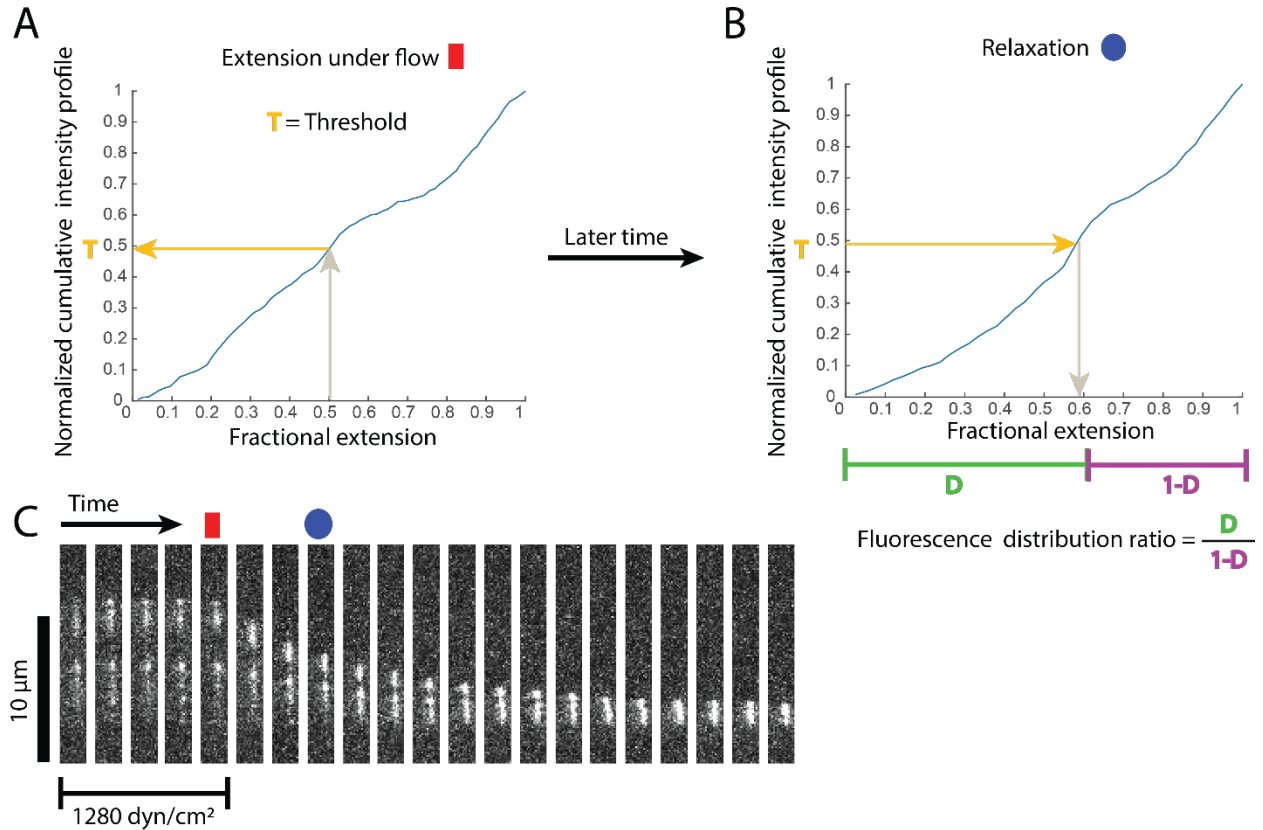
Supplemental Figure 8. Explanation of fluorescence distribution ratio for comparing relaxation conformations. A. The molecule is extended under flow at high shear (1280 dyn/cm^2). The cumulative intensity profile is found and normalized to one. For each extended molecule, the normalized cumulative intensity profile at 0.5 fractional extension is recorded as a specific threshold T (yellow). **B.** The flow is turned off and the molecules relax back down. On each frame, we find the fractional extension D (green) at which the normalized cumulative intensity profile is equal to the defined threshold T. The final value is a ratio of the value D over 1-D (purple). Simulations were analyzed in analogous way based on full xyz trajectories. **C.** Kymograph of VWF relaxation, with the region of interest shown for each frame as a function of time. Frames are 0.05 seconds apart. The Intensity plots in figure 5A is made from frame five (red square) while the flow is still on. The intensity plot in figure 5B (blue circle) is made from frame eight. Data was generously given from Fu et al[2].

Supplemental Figure 9. Conformation analysis of tethered polymer relaxation for different models and VWF with expanded lengths. Distribution ratio is calculated as explained in supplemental figure 5. **A**. Data reanalyzed from Fu et al.[2] looking at VWF relaxation from an extended state for different initial extensions when stretched under high shear (1280 dyn/cm^2). The number of molecules at each initial extension is [210, 156, 51, 5] for shortest through longest bins respectable. Distribution ratio calculated based on the relaxation for different lengths as a function of fractional extension for the original LJ model (**B**), the revised LJ model (**C**), and the uncollapsed polymer model (**D**). The legend lengths represent the theoretical contour length. N represents the number of total beads in the simulation, a is the bead radius, and u is the LJ interaction parameter. Error bars are based on the standard deviation at each point. For each simulations, 10 different trials occur for each model and length.